UNIVERSITY OF CALIFORNIA
Santa Barbara

Virtual Oscillator Controlled Inverters in a Microgrid Setting with Secondary Control and Energy Storage

A thesis submitted in partial satisfaction of the
requirements for the degree Master of Science
in Electrical and Computer Engineering

by

Celeste M B Bean

Committee in charge:
Professor Francesco Bullo, Chair
Professor Mahnoosh Alizadeh
Professor Joao Hespanha

September 2018

The thesis of Celeste M B Bean is approved.

Professor Joao Hespanha

Professor Mahnoosh Alizadeh

Professor Francesco Bullo, Committee Chair

June 2018

Acknowledgements

I would like to extend my sincerest gratitude to Professor Francesco Bullo for his guidance and to Dr. Brian Johnson for his interminable patience and for his sponsorship at the National Renewable Energy Laboratory. Thank you to my family for their unending support, to my friends who have shared with me the highs and lows, and to Bernadette, of whom I will be thinking always.

ABSTRACT

Virtual Oscillator Controlled Inverters in a Microgrid Setting with Secondary Control and Energy Storage

by

Celeste M B Bean

Building from existing work on Virtual Oscillator Control (VOC) [1], this reports details design, analysis, and simulation of a standalone inverter-based microgrid composed of variable renewable energy sources and battery storage. VOC for inverters relies on local voltage and frequency measurements to allow for proportional loading and voltage/frequency synchronization, presenting a real-time decentralized control strategy that mimics droop control characteristics. The design specifications, derivations, models, and simulations demonstrate that VOC can operate bidirectionally (producing and consuming power) for resistive and capacitive loads. The inverters are shown to operate in a variety of more complex settings than have previously been examined: in parallel, under fluctuating loads, and under noisy loads. To compensate for deviations in steady-state frequency and voltage, low-bandwidth communication in the form distributed averaging proportional integral (DAPI) [2] control is adapted, derived, and simulated for a VOC-based microgrid. Lastly,

battery models representing distributed Energy Storage Systems (ESS) are incorporated to demonstrate grid robustness in times of excess load relative to generation available.

Contents

Chapter 1

Introduction

1.1 Microgrids

The intensified deployment of renewable energy sources (RES) presents a promising strategy in the quest for a more sustainable, environmentally friendly, and fiscally sensible electricity supply. In comparison to standard centralized power generation, distributed energy resources (DERs) offer higher energy utilization, lower power transmission losses, more flexible installation, and less pollution [3]. By virtue of the precision with which their output can be controlled, traditional generation sources such as nuclear and fossil-fuel power plants simplify stability issue affecting the power grid. Although distributed

wind-turbine and photovoltaic (PV) generation sources present many opportunities, their ongoing penetration into power grids does introduce technical challenges as a result of their fluctuating and unpredictable short-term output. Balancing intermittent power generation with load demand at all times and at different time scales becomes increasingly difficult [4].

The dynamics of power grids composed of few, large centralized energy sources is fundamentally different from those of a grid composed of many small distributed sources, prompting the rise of so-called microgrids [5]. Microgrids are low voltage, comparatively small collections of DERs that interface with higher voltage, larger power grid interconnections. As a group of heterogeneous interconnected loads and generation sources "within clearly defined electrical boundaries that acts as a single controllable entity with respect to the grid," a microgrid can operate in either grid-connected mode or islanded-mode. In grid-connected mode, the microgrid acts like an aggregated node feeding and drawing from the larger power grid. In islanded-mode, the microgrid produces its own energy and services its loads independently of the grid [6].

The output of renewable energy sources is often direct current (DC) power, which is not immediately compatible with alternating current (AC) power grids. Interfacing requires the use of power inverters, which dynamically transform the generated DC power to the grid's AC power at the appropriate

voltage magnitude and frequency [7]. In addition to handling variations in loads, inverters must compensate for changing levels of generation from DERs [8]. Inverters interfacing between variable generation sources and grid-wide bus loads must be able to dynamically adjust their output to ensure synchronicity and convergence with the grid at large. It is onto these inverters that one can implement controllers to satisfy microgrid objectives of balancing load demand and power injection, stabilizing voltages and synchronizing inverter frequencies, and proportionally loading inverters [9]. In the interest of realistic implementation of a control system that satisfies these objectives, a microgrid's control strategy must operate on a time-scale fast enough to address noisy, fluctuating loads and generation in addition to doing so in a decentralized fashion that minimizes the microgrid's communication complexity.

1.2 Hierarchical Control

The responsibilities of grid management are separated according to requisite time scales and are organized into hierarchies of control. Primary control operates at the fastest time scale, greater than 1 Hz, and is responsible for balancing generation and demand while ensuring proportional load sharing, "synchronizing the AC voltage frequencies, and stabilizing their magnitudes"

[2]. Secondary control corrects for steady-state errors in voltage magnitudes and frequency and operates at a slightly slower time scale than primary control. Tertiary control broadly covers the establishment of fair load sharing among energy resources, along with global economic dispatch optimization over the network according to current energy markets [10]. Tertiary control can operate on the order of anywhere between hours and days.

The most popular primary control strategy is droop control, "which linearly trades off the inverter-voltage amplitude and frequency with real- and reactive power output" [1]. Essentially, as resistive load increases/decreases, frequency decreases/increases. Likewise as capacitive or inductive load increases/decreases, voltage magnitude decreases/increases. Intuitively, one can imagine the inversely-proportional relationship between the frequency of a rotating mass and the electrical active power output [11].

Droop control's active/reactive power decoupling is described by linear controllers that specify the inverter frequency ω_i and voltage magnitude V_i as

$$\omega_i = \omega_{nom} - m_i P_i \tag{1.1}$$

$$V_i = V_{nom} - n_i Q_i \tag{1.2}$$

where ω_{nom} and V_{nom} respectively describe the nominal frequency and voltage.

P_i and Q_i respectively represent the measured real and reactive power injections, and the coefficients m_i and n_i are gaina reflecting the droop coefficients [12].

Because droop control ensures proportional loading and synchronization of inverters in a decentralized fashion, it is a particularly attractive controller for microgrids. Proportional loading describes a framework in which each generation source contributes its "fair share" of the load. For example, if a 9 kW and a 1 kW inverter were servicing a load, the 9 kW inverter would contribute 90% of the required power while the 1 kW inverter would deliver 10% of the necessary power. Synchronization indicates that power injections all have the same voltage, frequency, and phase angle. The decentralized nature of droop control requires no communication between nodes and thus no overhead or centralized controlling authority; inverters query only locally available quantities.

As a proportional controller, droop control inevitably results in steady-state errors. Secondary control seeks to correct for this deviation from nominal operation and takes on a variety of forms. Lastly, tertiary control seeks to optimize grid operation from a myriad of perspectives, ranging from load shifting with energy storage systems, to game-theoretical behavior shaping, to "smart" devices to use energy more efficiently.

1.3 Problem Description

While droop control offers a solution to synchronize injections and proportionally share loads between inverters, it operates on a slower time scale than is necessary for interfacing with highly-noisy renewable energy sources. In *Synthesizing Virtual Oscillators to Control Islanded Inverters* by Brian Johnson *et al.*, the authors propose an elegant controller that mimics droop-like characteristics but, being implemented on a microcontroller, operates at much faster time scales. This Virtual Oscillator Control (VOC) inverter is detailed for the reader's reference in Chapter 2. These inverters have been rigorously analyzed in their basic operation and mimicry of droop-control but have not been modeled or simulated as extensively in more complex scenarios. This thesis seeks to more expansively demonstrate VOC performance in a microgrid setting.

1.4 Summary of Contributions

The objective of this thesis is to design, analyze, and simulate a self-sustaining inverter-based microgrid with Virtual Oscillator Control (VOC) in the presence of variable renewable generation and battery storage. Real-time decentralized controllers maintain system stability and, when necessary, rely on low-bandwidth distributed controllers to facilitate information exchanges. Lastly,

energy storage systems are modeled and controlled under different control scheme to maximize various performance criteria.

The contributions of this thesis are four-fold. Chapter 3 includes derivations and simulations of multiple VOC inverters with different ratings in parallel in cases of fluctuating loads and noisy loads. Chapter 4 details derivations and simulations of multiple VOC inverters equipped with a distributed averaging proportional integral (DAPI) secondary control strategy to correct steady state deviations from nominal system operation in ideal, noisy, and fluctuating generation and/or load cases. Chapter 5 deals with the derivation and simulation of multiple VOC inverters equipped with energy storage systems and comparisons of the performance of various control schemes.

Chapter 2

Virtual Oscillator Control

Included in this section is a summary of relevant information from *Synthesizing Virtual Oscillators to Control Islanded Inverters* by Brian Johnson *et al.* [1]. The work detailed in this thesis builds upon this initial characterization of a single Virtual Oscillator Control (VOC) to control an individual single-phase inverter. For justifications and derivations of the following implementation, readers are referred to the original publication. In the interest of brevity, the following results and derivations are included for reference only and will not be justified.

2.1 Benefits of Virtual Oscillator Control

Virtual Oscillator Control (VOC) is termed as such because the nonlinear oscillations of a Van der Pol oscillator are programmed onto a digital microcontroller. The microcontrollers then use sinusoidally varying oscillator states to construct pulse-width modulation (PWM) control signals that control the magnitude and frequency of the inverter's power injection, requiring only locally available information.

Previous work has detailed several advantages unique to VOC, justifications of which will be taken for granted in following sections of this work. In [13], the authors demonstrate "that droop laws are intrinsically embedded within a slower time scale in the nonlinear dynamics of Van der Pol oscillators" and prove synchronicity of distributed, communication-less system-wide amplitude and phase dynamics in a resistive network interconnecting inverters. In [14], the authors prove VOC's ability to converge to a stable sinusoidal steady state from arbitrary initial conditions and detail a technique for "seamless addition of inverters... into an energized system," which fits in with goals of "plug-and-play" technology. In [15], the authors show that synchronization occurs regardless of the number of oscillators and independently of the load on the system. In [16], the authors demonstrate synchronization from a cold

start and "the addition of an inverter to an already synchronized system."

The critical difference between VOC and droop control lies in the time-scales at which each control scheme operates. Droop control relies on phasorial electrical quantities, which instrinsically operate on "the notion of an electrical frequency that [is] only well defined on slow AC-cyle time scales" [1]. Droop control's reliance on phasors, which assume a quasi-stationary sinusoidal steady state, limit its ability to respond to intermediate deviations from steady-state. Because VOC acts on "instantaneous time-domain signals" rather than phasors, VOC-equipped inverters are able to "rapidly stabilize arbitrary initial conditions and load transients to a stable limit cycle" [1].

2.2 Controller Implementation

A digital microcontroller emulates the discretized dynamics of a Van der Pol oscillator to create a closed-loop controller. Figure 2.1, Figure 2 borrowed from [1], shows the circuit model of the virtual oscillator and its three parallel components, along with its implementation on a single-phase H-bridge invereter and an LCL filter to reduce high-order harmonics. From left to right: σ represents a negative-conductance element; inductance L and capacitance C together yield a resonant frequency of $\omega_{nom} = 1/\sqrt{(LC)}$; and α governs the

magnitude of a cubic voltage-dependent current source. The term v_C denotes the voltage across the virtual capacitor, while i_L refers to the current through the virtual inductor. The term αv_c^3 describes "the current consumed by the cubic voltage-dependent current source" [1]. To interface with the inverter, κ_i scales the current sampled from the inverter's output, and κ_v scales the output across the inverter to the nominal voltage magnitude.

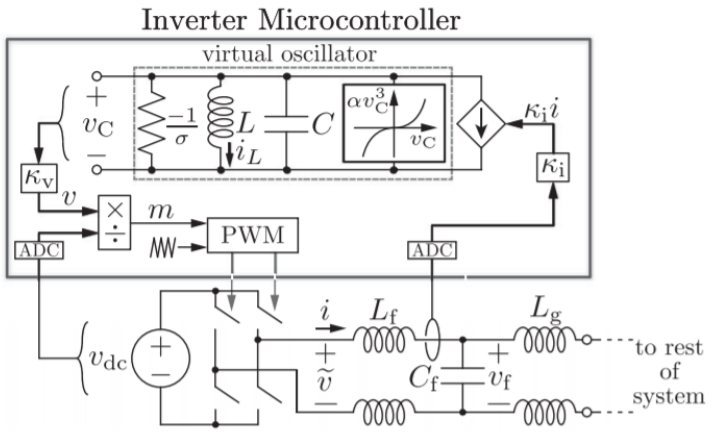

FIGURE 2.1: Figure 2 from [1]: "Implementation of VOC on a single-phase H-bridge inverter with an LCL filter."

Equation 2.1, reproduced equation (3) from [1], describes the dynamics of the virtual-oscillator inductor current i_L and inverter terminal voltage v

produced by a VO-controlled inverter.

$$\begin{aligned} L\tfrac{di_L}{dt} &= v \\ C\tfrac{dv}{dt} &= -\alpha\tfrac{v^3}{\kappa_v^2} + \sigma v - \kappa_v i_L - \kappa_v \kappa_i i \end{aligned} \tag{2.1}$$

Table 2.1 summarizes the AC performance specifications that the controller design parameters must satisfy. For each inverter, the rated real power $\bar{P}_{rated}$ quantifies the maximum real power that the inverter can contribute, and the rated reactive power $|\bar{Q}_{rated}|$ describes the maximum reactive power that the inverter can contribute. The nominal system frequency ω_{nom} is the frequency set point, and $|\Delta\omega|_{max}$ describes the maximum deviation allowable from ω_{nom}. Nominal RMS voltage $\bar{V}_{nom}$ describes the voltage magnitude set point, and open-circuit voltage $\bar{V}_{oc}$ describes the output voltage of an unloaded system. The voltage $\bar{V}_{min}$ corresponds to the minimal allowable voltage, achieved when the system is fully loaded. In accordance with the proportional droop control laws specified in equations (1.1) and (1.2) (recall the inverse relationship), as an inverter spans from its minimum to its maximum real power loading, it should sweep from [0 W, $\omega_{nom} + |\Delta\omega|_{max}$] to [$\bar{P}_{rated}$ W, $\omega_{nom} - |\Delta\omega|_{max}$]. Likewise, as an inverter spans from its minimum to its maximum reactive power loading, it should sweep from [0 VAR, $\bar{V}_{max}$] to [$\bar{P}_{rated}$ VAR, $\bar{V}_{min}$].

TABLE 2.1: AC Performance Specifications

Symbol	Description	Value	Units
$\bar{P}_{rated}$	Rated real power	750	W
$\lvert\bar{Q}_{rated}\rvert$	Rated reactive power	750	VARs
$\bar{V}_{nom}$	Nominal voltage	120	V (RMS)
$\bar{V}_{oc}$	Open-circuit voltage	126	V (RMS)
$\bar{V}_{min}$	Voltage at rated power	114	V (RMS)
ω_{nom}	Nominal system frequency	$2\pi 60$	rad/s
$\lvert\Delta\omega\rvert_{max}$	Maximum frequency offset	$2\pi 0.5$	rad/s
t_{rise}^{max}	Rise time	0.2	s
$\delta_{3:1}^{max}$	Ratio of third-to-first harmonic	2	%

Below are explanations of the adjustable parameters available to a control strategy using VOC and the process used to determine specific values for the design parameters, all of which are summarized in Table 2.2.

TABLE 2.2: VOC Parameters (Table 1, [1])

Symbol	Description	Given Value	Units
κ_v	Voltage-scaling factor	126	V/V
κ_i	Current-scaling factor	0.15	A/A
σ	Conductance	6.09	Ω^{-1}
α	Coefficient of cubic current source	4.06	A/V^3
C	Harmonic-oscillator capacitance	0.18	F
L	Harmonic-oscillator inductance	$3.99*10^{-5}$	H

The voltage-scaling factor κ_v scales the VOC output such that when the VO capacitor is 1 V RMS, the inverter-terminal voltage is equal to the open-circuit voltage V_{oc}:

$$\kappa_v = \bar{V}_{oc} \tag{2.2}$$

The current-scaling factor κ_i scales the VOC's loading such that when the inverter is loaded to full rated capacity $\bar{P}_{rated}$, the VO output current is 1 A:

$$\kappa_i = \frac{\bar{V}_{min}}{\bar{P}_{rated}} \tag{2.3}$$

The VO conductance σ reflects voltage regulation:

$$\sigma = \frac{\bar{V}_{oc}}{\bar{V}_{min}} \frac{\bar{V}_{oc}^2}{\bar{V}_{oc}^2 - \bar{V}_{min}^2} \tag{2.4}$$

The cubic coefficient of the nonlinear voltage-dependent current source α, in conjunction with the conductance σ, incorporates the maximum power value $\bar{P}_{rated}$:

$$\alpha = \frac{2\sigma}{3} \tag{2.5}$$

The frequency regulation characteristic described by the linear droop control relationship in 1.1, the rise time t_{rise}^{max}, and the ratio of amplitudes of the third harmonic to the fundamental $\delta_{3:1}^{max}$ all factor into the design constraints determining the harmonic oscillator capacitance C and inductance L:

$$\max\{C_{|\Delta\omega|_{max}}^{min}, C_{\delta_{3:1}}^{min}\} \leq C \leq C_{t_{rise}}^{max} \tag{2.6}$$

The inductance L follows from the capacitance C and nominal frequency ω_{nom}:

$$L = \frac{1}{C(\omega_{nom})^2} \tag{2.7}$$

2.3 Bidirectional Simulation

The established work in the previous section characterized a unidirectional inverter–that is, an inverter that had the capacity to contribute needed active power to the grid but not to consume excess active power from the grid.

A bidirectional inverter is attractive for a number of reasons. A generation source equipped with consumptive capacity can absorb power during periods of excess to, for example, charge an energy storage system, rather than simply curtailing its production. Such an inverter could also could useful for a microgrid operating in grid-connected mode.

Rederiving the design specifications in Table 2.2 to accept power requires adjusting the inverter's droop characteristics. The original parameter derivations assume that $0 \leq P_i \leq P_{rated,i}$. Instead of having only the parameters of nominal frequency ω_{nom}, rated power $\bar{P}_{rated}$, and frequency at rated power ω_{min}, one can incorporate new parameters of maximum rated power $\bar{P}_{rated}$ and minimum rated power $\bar{P}_{min}$, with frequency at each of these loadings of ω_{max} and ω_{min}, respectively. Effectively, this requires a shift of the y-intercept on the droop controllers.

To demonstrate the operation of these bidirectional inverters, we turn to simulations. Resistive loads dissipate real power, while capacitive and inductive loads dissipate reactive power. We will use each of these loads to demonstrate the inverters' operation under a spectrum of loading demands. Define the instantaneous active- and reactive-power injections as [17]:

$$P(t) = v(t)i(t) \tag{2.8}$$

$$Q(t) = v(t - \pi/2)i(t) \tag{2.9}$$

To simulate a microgrid as the load sweeping the spectrum of real and reactive power ratings, we simulate resistive and capacitive loads.

To characterize the load current of a resistive load, begin with KVL analysis on a single inverter attached to a purely resistive load, depicted in Figure 2.2:

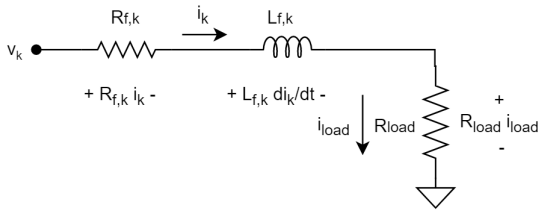

FIGURE 2.2: A single inverter attached to a purely resistive load

In the case of the single inverter, $i_{load} = i_k$. The following equations describe KVL, manipulated to isolate for inverter output current i_k, which is an input to the VOC:

$$v_k = R_{f,k}i_k + L_{f,k}i_k s + R_{load}i_{load} \tag{2.10}$$

$$v_k = R_{f,k}i_k + L_{f,k}i_k s + R_{load}i_k \tag{2.11}$$

$$L_{f,k}i_k s = v_k - R_{f,k}i_k - R_{load}i_k \tag{2.12}$$

$$i_k = \frac{1}{s}\frac{1}{L_{f,k}}(v_k - R_{f,k}i_k - R_{load}i_k) \tag{2.13}$$

$$i_k = \frac{1}{s}\frac{1}{L_{f,k}}(v_k - (R_{f,k} + R_{load})i_k) \tag{2.14}$$

Finally, the grid-tied resistor and inductor must be scaled relative to the maximum power rating:

$$R_{f,i} = 1/(P_{rated,max,i}/750) \tag{2.15}$$

$$L_{f,i} = 0.0001/(P_{rated,max,i}/750) \tag{2.16}$$

Figure 2.3 shows the steady-state simulation results for a single bidirectional inverter connected to a purely resistive load as shown in Figure 2.2. In each simulation, the inverter services an unchanging load indicated along the x-axis, demonstrating adherence to droop control.

Similarly, attaching instead to a capactive load (simply substituting C_{load} for R_{load} in 2.2) results in the following relationship. Recall that

$$i_c(t) = C\frac{dv_c(t)}{dt} \implies v_c(t) = \frac{1}{C}\int i_c(t) \tag{2.17}$$

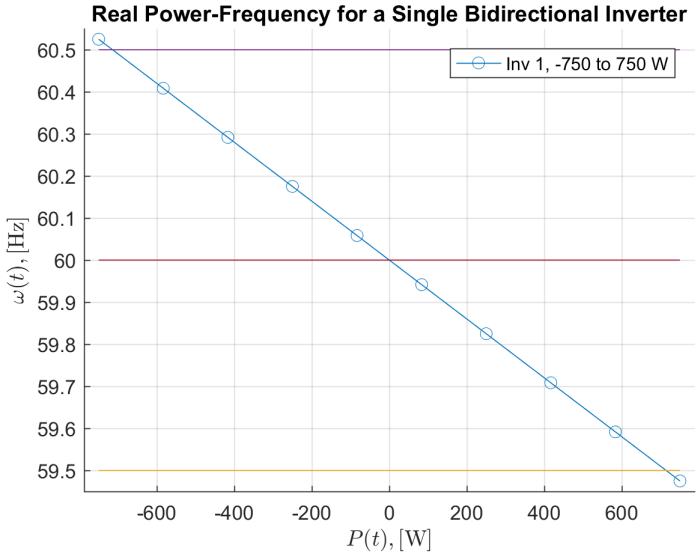

FIGURE 2.3: Resistive load sweep for a single bidirectional inverter

The following equations describe KVL, manipulated to isolate for inverter output current i_k, which is an input to the VOC:

$$v_k = R_{f,k} i_k + L_{f,k} i_k s + \frac{1}{s} \frac{1}{C_{load}} i_{load} \tag{2.18}$$

$$v_k = R_{f,k} i_k + L_{f,k} i_k s + \frac{1}{s} \frac{1}{C_{load}} i_k \tag{2.19}$$

$$L_{f,k} i_k s = v_k - R_{f,k} i_k - \frac{1}{s} \frac{1}{C_{load}} i_k \tag{2.20}$$

$$i_k = \frac{1}{s} \frac{1}{L_{f,k}} (v_k - R_{f,k} i_k - \frac{1}{s} \frac{1}{C_{load}} i_k) \tag{2.21}$$

$$i_k = \frac{1}{s} \frac{1}{L_{f,k}} (v_k - (R_{f,k} + \frac{1}{s} \frac{1}{C_{load}}) i_k) \tag{2.22}$$

As for the capacitive load, Figure 2.4 shows the steady-state simulation

results for a single bidirectional inverter connected to a capacitive load. In each simulation, the inverter services an unchanging load of the power indicated along the x-axis, demonstrating adherence to droop control.

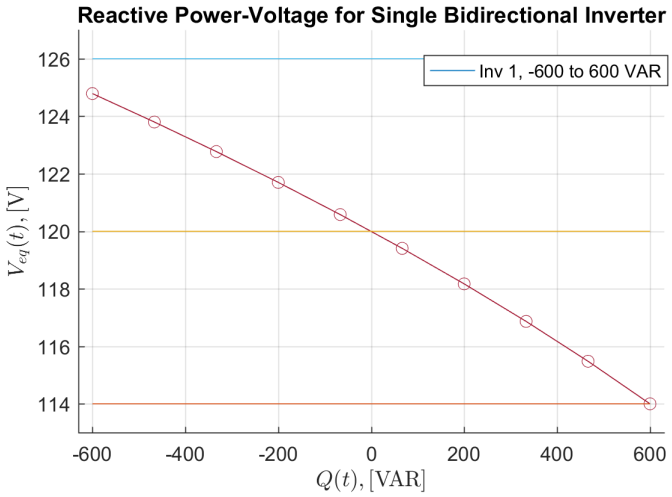

FIGURE 2.4: Capacitive load sweep for a single bidirectional inverter

Chapter 3

Microgrid Simulations

The organization of each section includes a motivation for the scenario to be simulated, a derivation of the new or adjusted parameters, and simulation results for the given circumstances in both individual examinations and steady-state frequency sweeps. Time-averaged models are included when appropriate.

Because the microgrid is assumed to be self-powered, excess loads, which would be modeled as negative load power, are not simulated. Instead inverters and the power from their associated generation sources are curtailed, rather than having the inverters consume power from the grid.

3.1 Parallel

Conceptually, a microgrid is simply a collection of inverters connected in parallel to a single bus load. Arranging inverters in parallel to satisfy a load increases the microgrid's power ratings, following the same principles that govern battery banks in series and in parallel. Numerous smaller decentralized inverters, like a neighborhood equipped with solar panels, offer a more diversified, robust interconnection compared to fewer large centralized inverters, such as a suburb supplied by a coal-fired power plants. If a single inverter fails, the latter system may experience a power outage, whereas in a distributed case, "(n-1) modules [remain to] deliver the needed power to the load" [8].

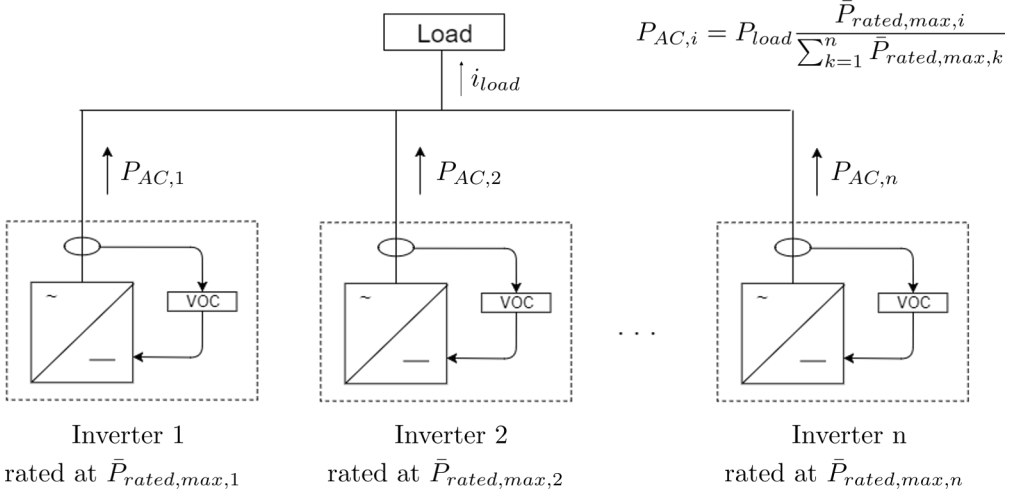

FIGURE 3.1: Figure illustrating multiple VOC inverters interfacing with a single load.

Because the inverters all connect in parallel to satisfy a single load on a bus, illustrated by Figure 3.1, the load current is simply the sum of all of the individual inverters' currents:

$$i_{load} = \sum_{i=1}^{n} i_k \tag{3.1}$$

The following equations describe KVL, manipulated to isolate for inverter output current i_k, which is an input to the VOC:

$$v_k = R_{f,k} i_k + L_{f,k} \frac{i_k}{s} + R_{load} i_{load} \tag{3.2}$$

$$L_{f,k} \frac{di_k}{dt} = v_k - R_{f,k} i_k - R_{load} i_{load} \tag{3.3}$$

$$i_k = \frac{1}{s} \frac{1}{L_{f,k}} (v_k - R_{f,k} i_k - R_{load} i_{load}) \tag{3.4}$$

Derivations for including a purely capacitive load are below. Recall that

$$i_c(t) = C \frac{dv_c(t)}{dt} \implies v_c(t) = \frac{1}{C} \int i_c(t) \tag{3.5}$$

The following equations describe KVL, manipulated to isolate for inverter output current i_k, which is an input to the VOC:

$$v_k = R_{f,k} i_k + L_{f,k} \frac{i_k}{s} + \frac{1}{s} \frac{1}{C_{load}} i_{load} \tag{3.6}$$

$$L_{f,k} \frac{di_k}{dt} = v_k - R_{f,k} i_k - \frac{1}{s} \frac{1}{C_{load}} i_{load} \tag{3.7}$$

$$i_k = \frac{1}{s} \frac{1}{L_{f,k}} (v_k - R_{f,k} i_k - \frac{1}{s} \frac{1}{C_{load}} i_{load}) \tag{3.8}$$

$$i_{load} = C_{load} \frac{dv_{bus}}{dt} = \sum_{k=1}^{n} i_k \tag{3.9}$$

$$v_{bus} = \frac{1}{C_{load}} \int i_{load} \tag{3.10}$$

3.2 General Simulation Setup

The following simulations model four inverters with the following specifications, in which inverter 4 is twice as large as inverter 1:

TABLE 3.1: Inverter specifications

Inverter	$[\bar{P}_{rated,min,i},\ \bar{P}_{rated,max,i}]$	$[\bar{Q}_{rated,min,i},\ \bar{Q}_{rated,max,i}]$
1	[-750 W, 750 W]	[-600 VAR, 600 VAR]
2	[-1000 W, 1000 W]	[-800 VAR, 800 VAR]
3	[-1250 W, 1250 W]	[-1000 VAR, 1000 VAR]
4	[-1500 W, 1500 W]	[-1200 VAR, 1200 VAR]

Each simulation represents 2 days (48 hours), with a representative sampling time of 10 Hz. As such, the Simulink simulations use a variable step size solver with a maximum step size of $\frac{1}{36000}$. The simulations shown reflect load data modelled from [18]. Fluctuating loads show the same time-varying demand. Note that these simulations assume total availability of generation sources (i.e., it is taken for granted that power will be available). Managing the total availability of power falls into the wheelhouse of tertiary control, a form of which is discussed in Chapter 5.

The following plots will be organized into four subplots. The first subplot shows the demanded load, the contributions of each inverter, and the delivered load (the sum of the individual inverters). The second subplot illustrates percent error between the power demanded P_{load} and the power delivered $P_{delivered}$, found as:

$$error\% = \frac{P_{load} - P_{delivered}}{P_{load}} * 100\%$$

The third subplot shows the frequency or voltage fluctations for resistive and capacitive loads, respectively, and the fourth subplot shows synchronization error as measured by the metric $||\Pi v||_{n+1}$ established in [1], where $n+1$ is the number of inverters n in addition to the cumulative delivered power. In the given procedure, $v = [v_1, ...v_{n+1}]^T$ collected terminal voltages at the inverters and load bus, and the projection matrix Π is defined as $\Pi := I_{n+1} - \frac{1}{n+1} 1_{n+1} 1_{n+1}^T$. $I_{(n+1)\times(n+1)}$ is the $(n+1) \times (n+1)$ identity matrix, and $1_{(n+1)\times(1)}$ is the $(n+1) \times 1$ vector with all entries equal to one. The values given by $||\Pi v||_{(n+1)}$ "returns a vector where the entries capture deviations from the average of the vector v" [16].

3.3 Fluctuating Load

Simulating the inverters' parallel configuration demonstrates the system's response to a time-varying input which spans the upper and lower limits of the system. The physically meaningful interpretation is a microgrid with changing demand according to the time of day, for example, peaking in the evening when people return home and reaching a nadir very late at night.

For a resistive load, the inverters track the changing demand in both real power injection and frequency synchronization. Figure 3.2 shows simulations

that demonstrate this behavior.

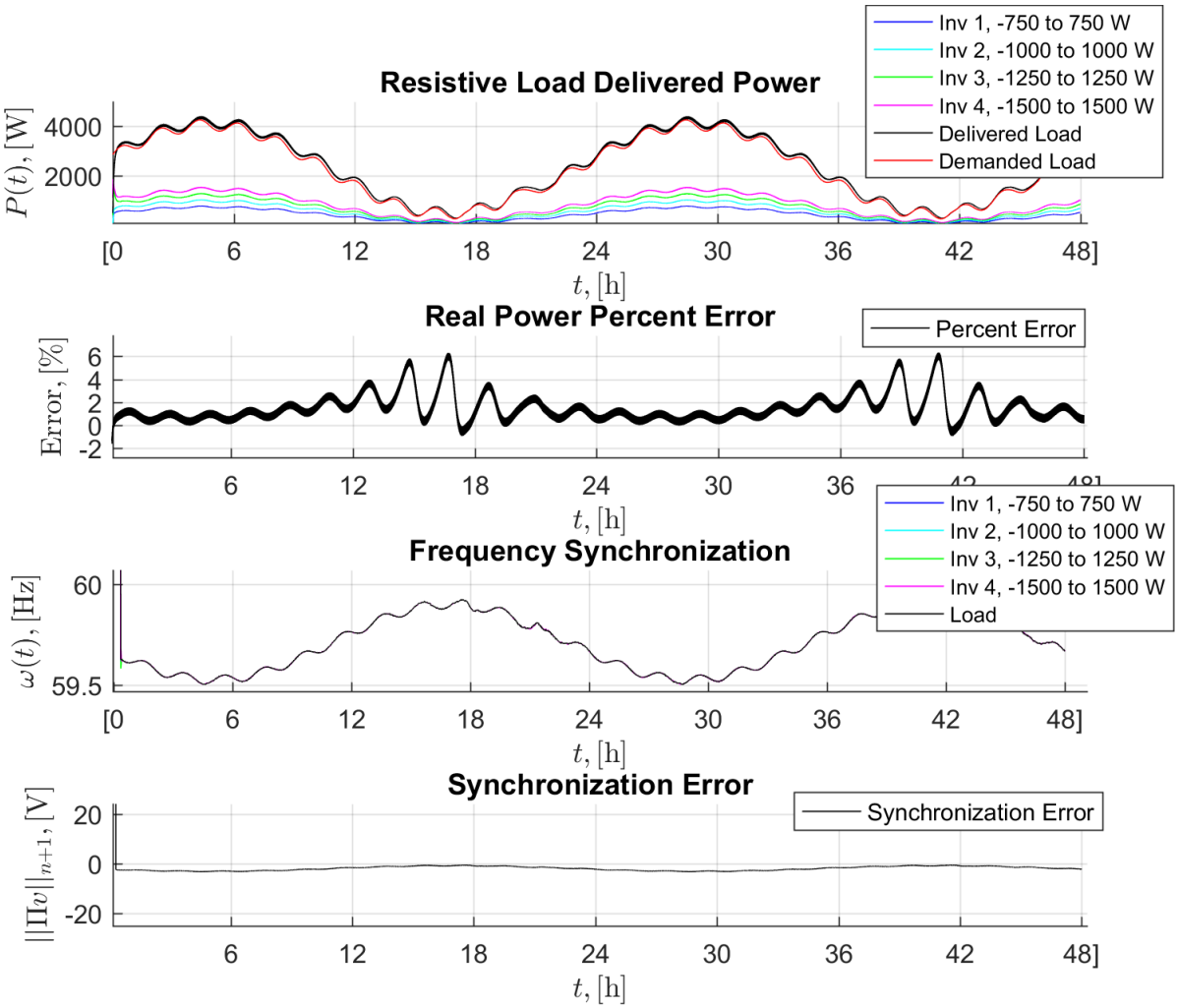

FIGURE 3.2: Simulation results of a fluctuating resistive load.

The first subplot shows the demanded active power in red, fluctuating according to one sine wave at a slow frequency and another at a higher frequency. The RMS delivered active power in black is the sum of the individual

loads, shown in multiple colors with their respective ratings. The individual inverters demonstrate nominal proportional load sharing: the largest inverter, rated at 1500 W, contributes twice as much power as the smallest inverter, rated at 750 W.

The second subplot shows the error between demanded load and delivered load and demonstrates the the error remains below 6% for the full spectrum of power demands. As the plot indicates, the relative percent error is well within acceptable margins.

The third subplot illustrates the frequency of the AC power of the delivered real power and from each inverter. The frequency sweeps from 60 degrees to 59.5 degrees, inversely proportionally to the load demanded, in accordance with expectations.

The fourth subplot shows synchronization error $||\Pi v||_{(n+1)}$, as described by the formulation in the beginning of this section, which converges to 0 in less than a second.

For a capacitive load, the inverters track the changing demand in both reactive power injection and voltage magnitude synchronization. Figure 3.3 shows simulations that demonstrate this behavior.

The first subplot shows the demanded reactive power in red, fluctuating

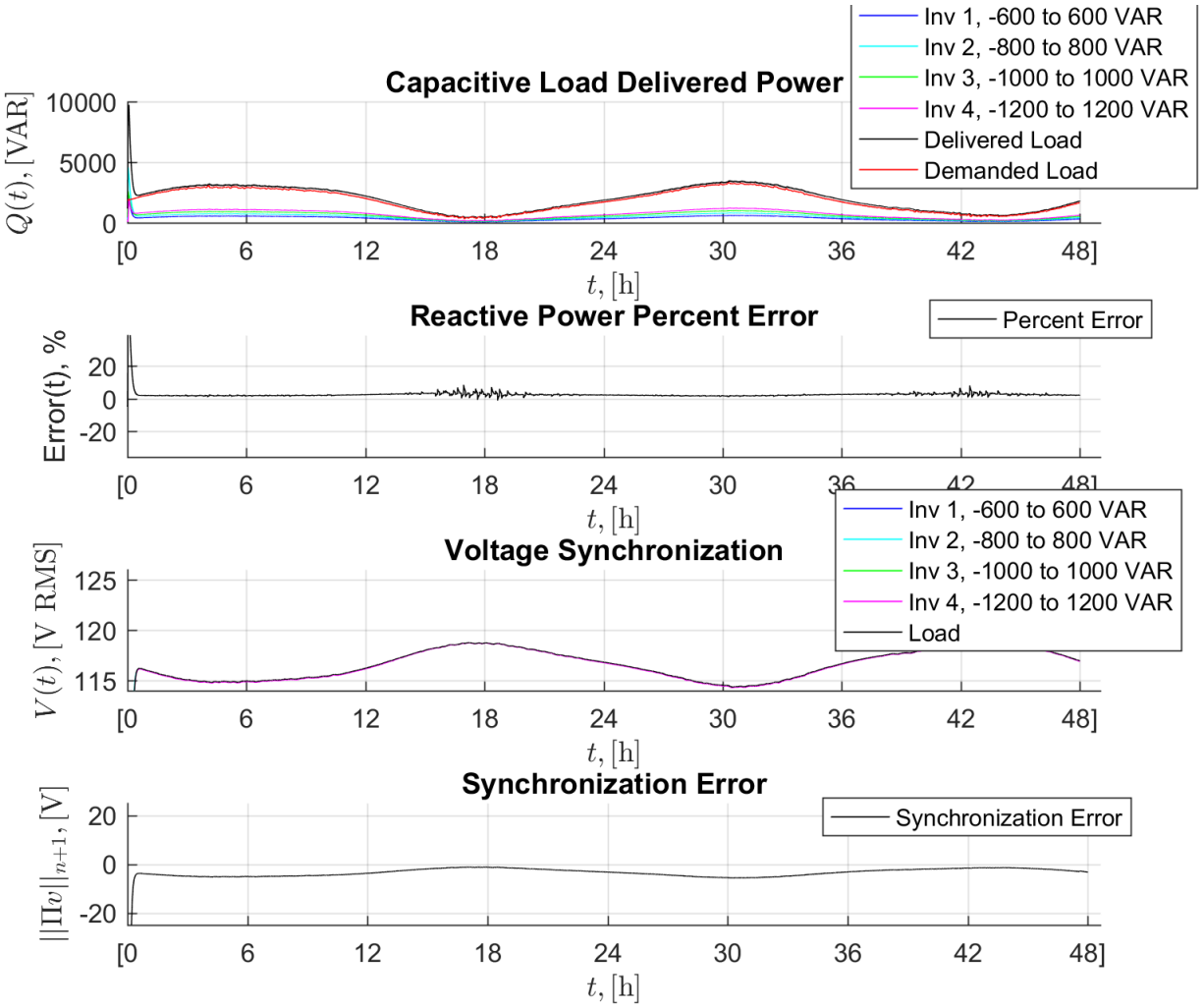

FIGURE 3.3: Simulation results of a fluctuating capacitive load.

as before. The RMS delivered active power in black is the sum of the individual loads, shown in multiple colors with their respective ratings. The individual inverters demonstrate nominal proportional load sharing: the largest inverter, rated at 1200 VAR, contributes twice as much power as the smallest inverter,

rated at 600 VAR. The second subplot shows minimal error. In the third subplot, all of the voltages' magnitudes synchronize and inversely track the demanding load. The fourth subplot shows synchronization error $||\Pi v||_{(n+1)}$, as described by the formulation in the beginning of this section.

3.4 Noisy Load

"Noisy" loads show the same time-varying generation but also include dramatic stochastic fluctuations to reflect the noise of photovoltaic generation sources. The distinction is important because correct operation in the presence of noise demands the speed and robustness of the inverters' control in even more adversarial conditions.

Figure 3.4 shows the results of a simulation demonstrating four parallel inverters' response to a noisy, fluctuating resistive load. This scenario more realistically reflects the operating circumstances of a real microgrid in which random variations complicate the control schemes, but the VOC-equipped inverters still demonstrate less than 15% error in the load that they deliver, relative to the demanded error. It is also important to note that the worst error occurs most dramatically during periods of minimal loading, in which the noise itself is more dramatic, relative to the demanded load.

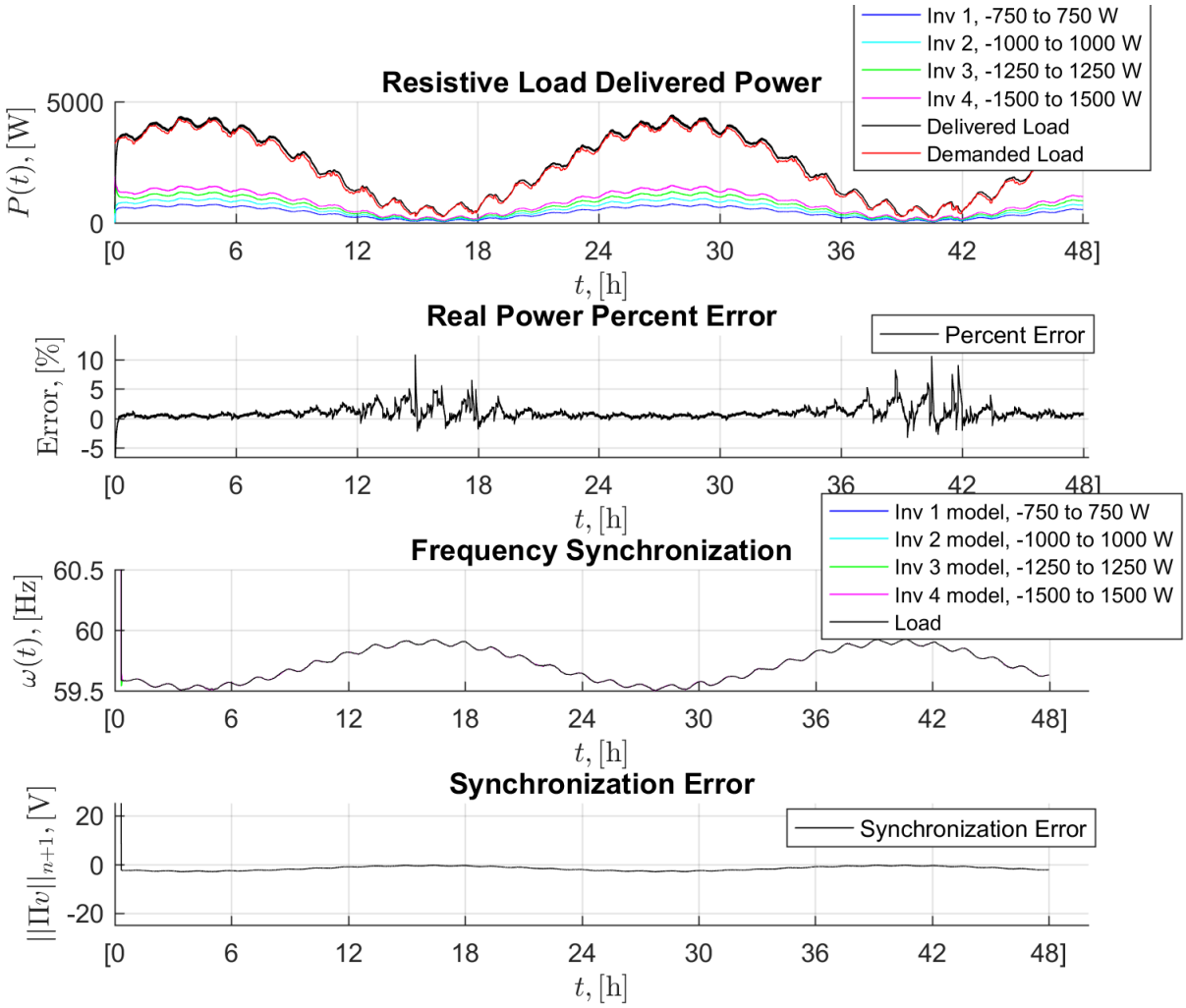

FIGURE 3.4: Simulation results of a noisy, fluctuating resistive load.

Figure 3.5 shows the results of a simulation demonstrating four parallel inverters' response to a noisy, fluctuating capacitive load. As with the resisitive load, the inverters deliver reactive power with limited error.

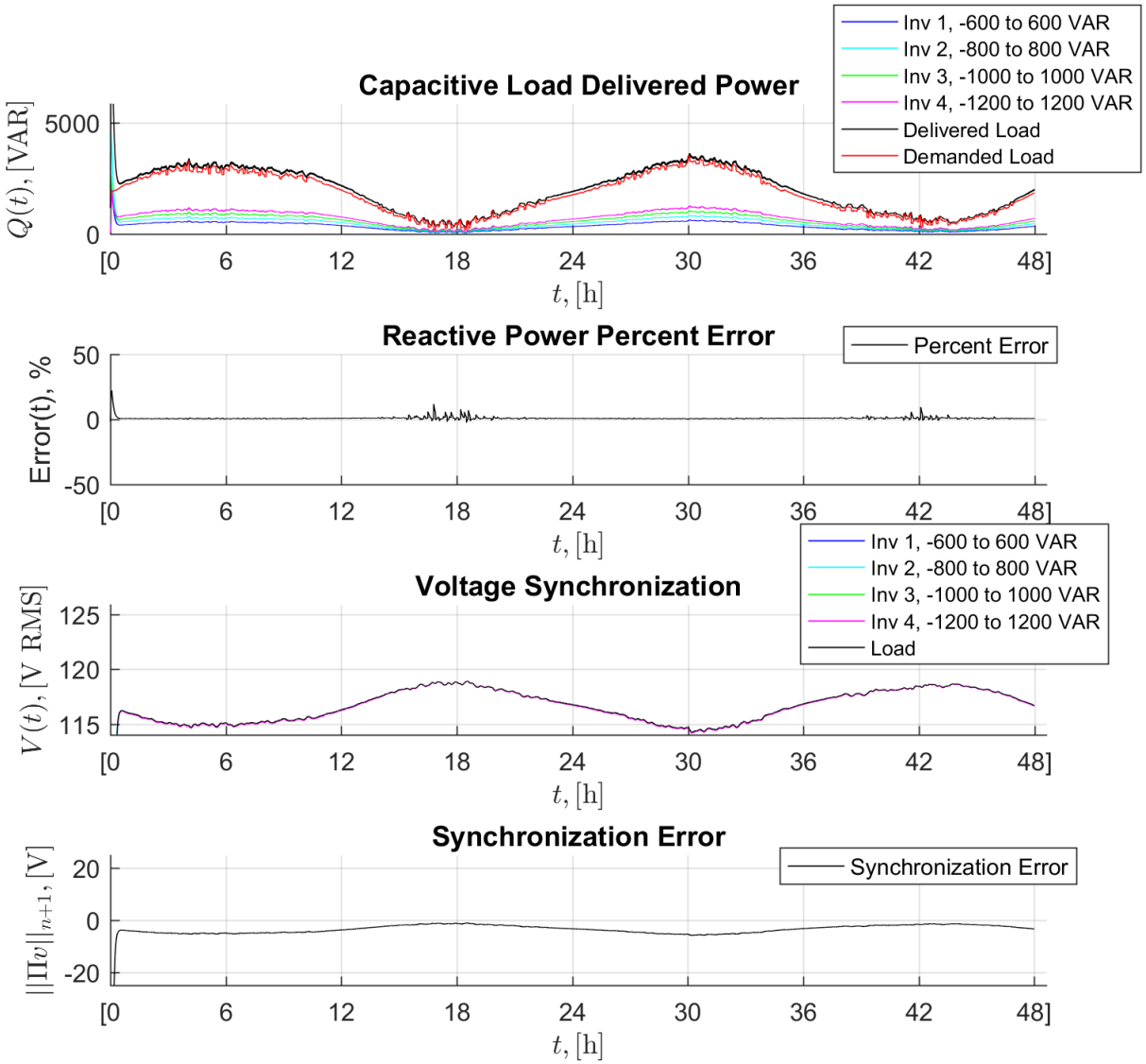

FIGURE 3.5: Simulation results of a noisy, fluctuating capacitive load.

Chapter 4

Secondary Control

In grid management, the responsibility of primary control is "[balancing] generation and demand, ... sharing the load, synchronizing the AC voltage frequencies, and stabilizing their magnitudes" [2]. Traditionally droop control has been used to achieve these goals, and as explained in the previous sections, VOC demonstrates droop-like characteristics and performs well in variety of simulated scenarios.

While decentralized primary control is quite elegant and satisfies microgrids' objectives of proportional loading, frequency synchronization, and autonomous control, VOC and droop control do result in steady-state error. In other words, the inverters' outputs will all synchronize to the same steady state

frequency ω_{ss} and steady state voltage V_{ss}, but these frequencies and voltages can converge to values within a margin around nominal frequency ω_{nom} and nominal voltage V_{nom}. Operating within this allowable margin is theoretically acceptable for grid operation but poses risks and compromises robustness in the event of grid fluctuations as the margin for error is decreased.

There are a number of options to correct this steady-state error in systems with droop controllers, and the reduction of this error is achieved via secondary control, which operates on a slower time scale than primary control. Older methods of secondary control use automatic generation control (AGC) or mimicries, in which a few geographically favourable generators "balance local generation in each area with load and inter-area power transfers" [2]. This method requires a centralized integral controller and can often compromise the proportional loading that initially made droop control attractive as a primary controller.

To align more closely with microgrids' ethos of decentralized control for distributed generation sources, we investigate the use of a Distributed Averaging Proportional Interal (DAPI) controller, imposed on VOC inverters [12]. The authors who propose the DAPI controller also give a detailed discussion of stability in the companion work of [10]. Their analysis, verified by experimental results, indicates that while secondary control typically operates at a

considerably slow time scale than primary control, DAPI can "be performed on similar time scales [to primary control] without stability issues or performance degradation" [12]. As such, the following discussion will not include stability analysis.

4.1 Continuous-Time Distributed Averaging

For a description of continuous-time distributed averaging, we borrow heavily from the description in [12]. A weighted undirected graph $G(\mathcal{V}, \mathcal{E}, \mathcal{A})$ describes the communication layer between distributed generators, where $\mathcal{V} = \{1, 2, ...\}$ is a labeling of the DGs, $\mathcal{E} \subseteq \mathcal{V} \times \mathcal{V}$ is the set of communication links, and A is the $n \times n$ weighted adjacency matrix of the graph, with elements $a_{ij} = a_{ji} \geq 0$. The edge $(i, j) \in \mathcal{E}$ if node i communicates with node j, and in that case $a_{ij} > 0$. Each node $i \in \{1, ..., n\}$ is associated with a scalar value x_i. The continuous-time distributed averaging or "consensus" updating rule for node i is given by equation (4) from [12]:

$$\dot{x}_i = -\sum_{j=1}^{n} a_{ij}(x_i - x_j) \tag{4.1}$$

Equation (5) from [12] rearranges equation (4), substituting the convex weight $w_{ij} = a_{ij}/(\sum_{j=1}^{n} a_{ij})$:

$$\frac{1}{\sum_{j=1}^{n} a_{ij}} \dot{x}_i = -x_i + \sum_{j=1}^{n} w_{ij} x_j \tag{4.2}$$

Under this averaging, the values x_i and x_j and neighboring nodes i and j converge. We now apply these ideas from continuous-time distributed averaging to microgrid control, with the intention of correcting for steady-state deviations from nominal voltage present in droop control. Figure 4.1 illustrates DAPI's integration into the parallel inverters simulated in Chapter 3.

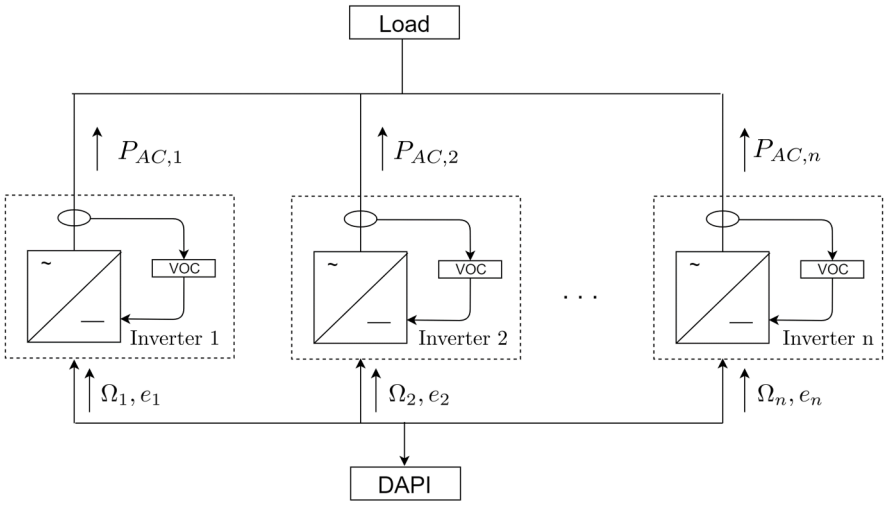

FIGURE 4.1: Distributed averaging proportional integral (DAPI) controller with multiple VOC inverters interfacing with a single load.

4.2 Frequency Regulation

Incorporating distributed averaging proportional integral control defined for droop control into a VOC requires absorbing DAPI variables into the adjustable VOC parameters. To begin, recall real power-frequency droop tradeoff:

$$\omega_i = \omega_{nom} - m_i P_i \tag{1.1}$$

where ω_i is inverter i's output frequency, ω_{nom} is the nominal system frquency, m_i is inverter i's droop coefficient, and P_i is the measured real power at the terminal connecting inverter i and the system.

To find the droop coeffient m_i in equivalent VOC terms, begin with equation (13) from [16]:

$$\omega_i - \omega_{nom} - \frac{\kappa_v \kappa_i}{2C\bar{V}_i^2}\bar{P}_{eq} = 0 \tag{4.3}$$

where κ_v represents the voltage scaling factor, κ_i represents the current scaling factor, C is the harmonic-oscillator capacitance, and V_i is the inverter's output voltage. Solving for ω_i gives:

$$\omega_i = \omega_{nom} - \frac{\kappa_v \kappa_i}{2C\bar{V}_i^2}\bar{P}_{eq} \tag{4.4}$$

In comparing equations 1.1 and 4.4, one can equate the droop coeffient m_i

with VOC parameters that give much more flexibility in dynamically tuning the system:

$$\frac{\kappa_v \kappa_i}{2C\bar{V}_i^2} = m_i \tag{4.5}$$

Having established the droop coefficient in terms of readily adjusted VOC parameters, secondary control literature that is applicable to droop controlled inverters becomes available to VOC systems. A secondary controller of particular interest is the distributed averaging proportional integral control proposed in [12] for reasons described in the beginning of this section.

Assume the nodes of the system are connected by a communication layer in the form of weighted adjacency matrix A, with elements $a_{ij} = a_{ji} \geq 0$ describing the commuiciation network between nodes i and j. Begin with equations (6a) and (6b) from [12]:

$$\omega_i = \omega_{nom} - m_i \bar{P}_i - \Omega_i \tag{4.6}$$

$$\frac{d\Omega_i}{dt} = -\frac{1}{f_i}(\omega_i - \omega_{nom}) - \sum_{j=1}^{n} a_{ij}(\Omega_i - \Omega_j) \tag{4.7}$$

The first equation 4.6 is simply the frequency droop equation 1.1 with a secondary control variable Ω_i. The second equation 4.7 describes the dynamics

of the secondary controller, where f_i is a positive gain and a_{ij} refers to an element in the symmetric weighted adjacency matrix A. Qualitatively, f_i affects the speed of frequency regulation at node i, and a_{ij} determines the speed of power sharing between nodes i and j.

The first term $(\omega_i - \omega_{nom})$ contributes an integral of the local frequency error. Including the diffusive averaging term $\sum_{j=1}^{n} a_{ij}(\Omega_i - \Omega_j)$ forces all of the secondary control variables to reach a consensus on the magnitude by which to shift each inverter's droop curve. While theoretically a system with only the first term might converge, in this case the secondary control variables Ω_i may "converge to different values and shift their respective droop curves by different amounts" without the second consensus term $\sum_{j=1}^{n} a_{ij}(\Omega_i - \Omega_j)$ [12]. The controller gains f_i and a_{ij} influence the controller's transient behavior but do not affect the performance with respect to proportional loading. By coordinating the shift in each node's droop curves, the consensus term maintains active power sharing. Intuitively, this can be imagined as adjusting the system set point so that the droop curve intersects with nominal frequency at any loading.

Consolidating equation 4.5, which describes the droop curve in terms of

VOC parameters, and equations 4.6 and 4.7, which outlines the DAPI controller, result in the following DAPI controller for a VOC-based system:

$$\omega_i = \omega_{nom} - \frac{\kappa_v \kappa_i}{2C\bar{V}_i^2}\bar{P}_i - \Omega_i \tag{4.8}$$

$$\frac{d\Omega_i}{dt} = -\frac{1}{f_i}(\omega_i - \omega_{nom}) - \sum_{j=1}^{n} a_{ij}(\Omega_i - \Omega_j) \tag{4.9}$$

Given that the nominal frequency ω_{nom} is a function of the harmonic-oscillator capacitance C and harmonic-oscillator inductance L VOC parameters, adjustments to the frequency set point can be absorbed into the capacitor and inductor terms. Recall the relationship between capacitance C, inductance L, and nominal frequency ω_{nom} given in equation (2.7) and rearranged below:

$$\omega_{nom} = \frac{1}{\sqrt{LC}} \tag{4.10}$$

Assume that the parameters that produce the nominal frequency are L_{nom} and C_{nom}. Because the VOC follows a droop curve, the actual system output deviates, but by absorbing the each node's local error contained in the secondary control variable Ω_i in adjustable VOC parameters, the nodes can coordinate their return to nominal frequency. Because L is a function of C, one can hold C constant and adjust L. Substituting these values into (4.8) results in:

$$\frac{1}{\sqrt{L_{adjustable}C_{nom}}} = \frac{1}{\sqrt{L_{nom}C_{nom}}} - \frac{\kappa_v\kappa_i}{2C\bar{V}_i^2}\bar{P}_i + \Omega_i \tag{4.11}$$

$$L_{adjustable}C_{nom} = \left(\frac{1}{\frac{1}{\sqrt{L_{nom}C_{nom}}} + \frac{\kappa_v\kappa_i}{2CV_{eq}^2}P_{eq} + \Omega_i}\right)^2 \tag{4.12}$$

$$L_{adjustable} = \frac{1}{C_{nom}(\frac{1}{\sqrt{L_{nom}C_{nom}}} + \frac{\kappa_v\kappa_i}{2CV_{eq}^2}P_{eq} + \Omega_i)^2} \tag{4.13}$$

To incorporate this into simulation, each inverter must add a communication bus that carries information about other nodes' secondary control variable. Doing so results in the following simulation shown in Figure 4.2. The simulation includes four inverters of different ratings as in the scenario simulated in Chapter 3, but in these simulations, DAPI with a gain of $f_i = 1$ turns on at $t = 3$ seconds to correct for frequency deviations from nominal. The first subplot shows the power contributions of all four inverters to a fluctuating load and demonstrates that load sharing is preserved, and the second subplot shows that error between demanded and delivered load remains minimal. The third subplot contains the most interesting information, demonstrating that the secondary controller does in practice drive the load's and all of the inverters' to the nominal frequency $\omega_{nom} = 60$ Hz, and the fourth subplot shows the error in synchronization, which is less than that seen in simulations with only primary control. The same simulation but with an aggressive noise profile is

simulated in Figure 4.3 and with a more aggressive DAPI gain of $f_i = \frac{1}{10}$ in Figure 4.4.

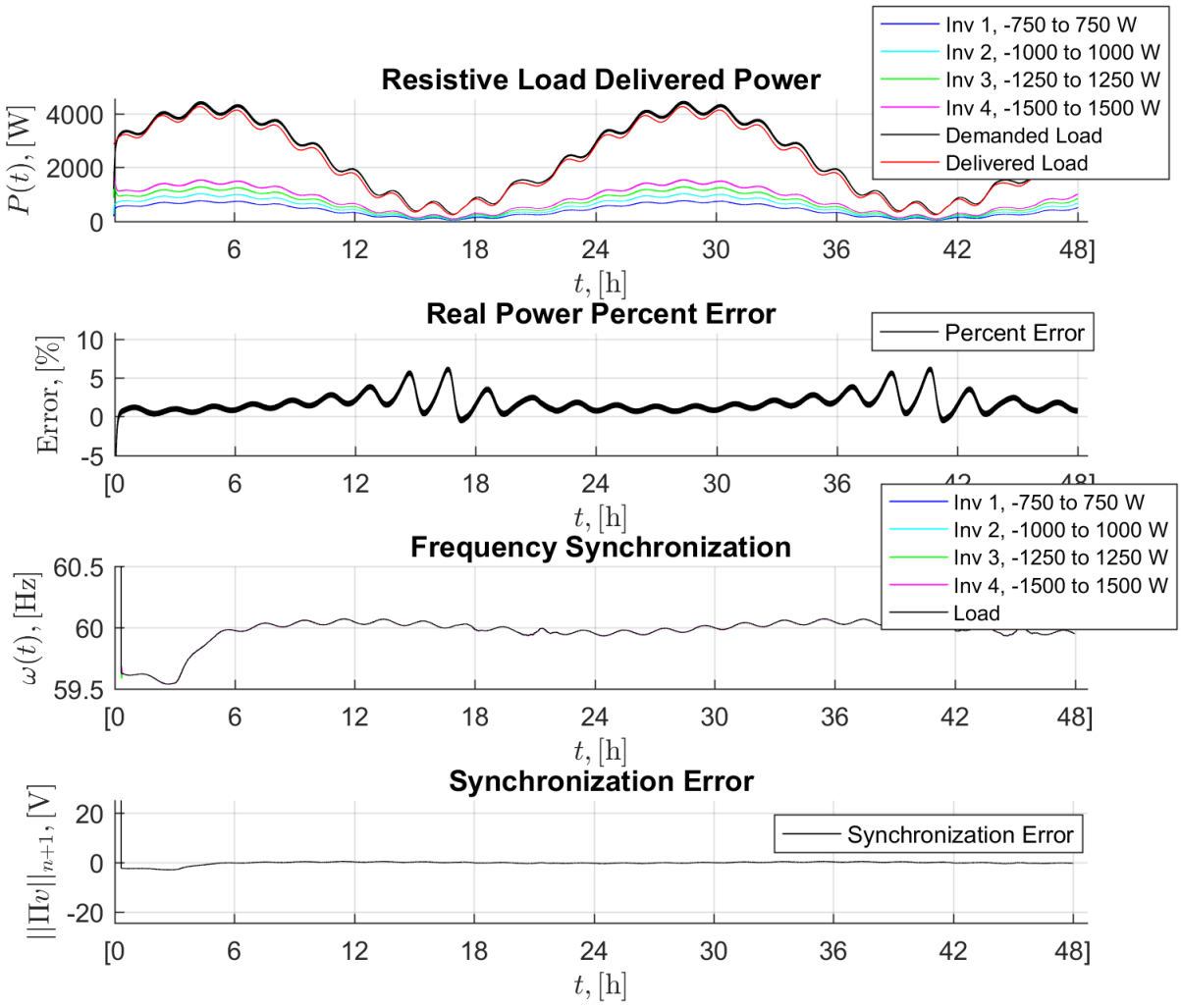

FIGURE 4.2: Simulation of four inverters under varying load with DAPI control, demonstrating synchronicity and return to nominal frequency ω_{nom}

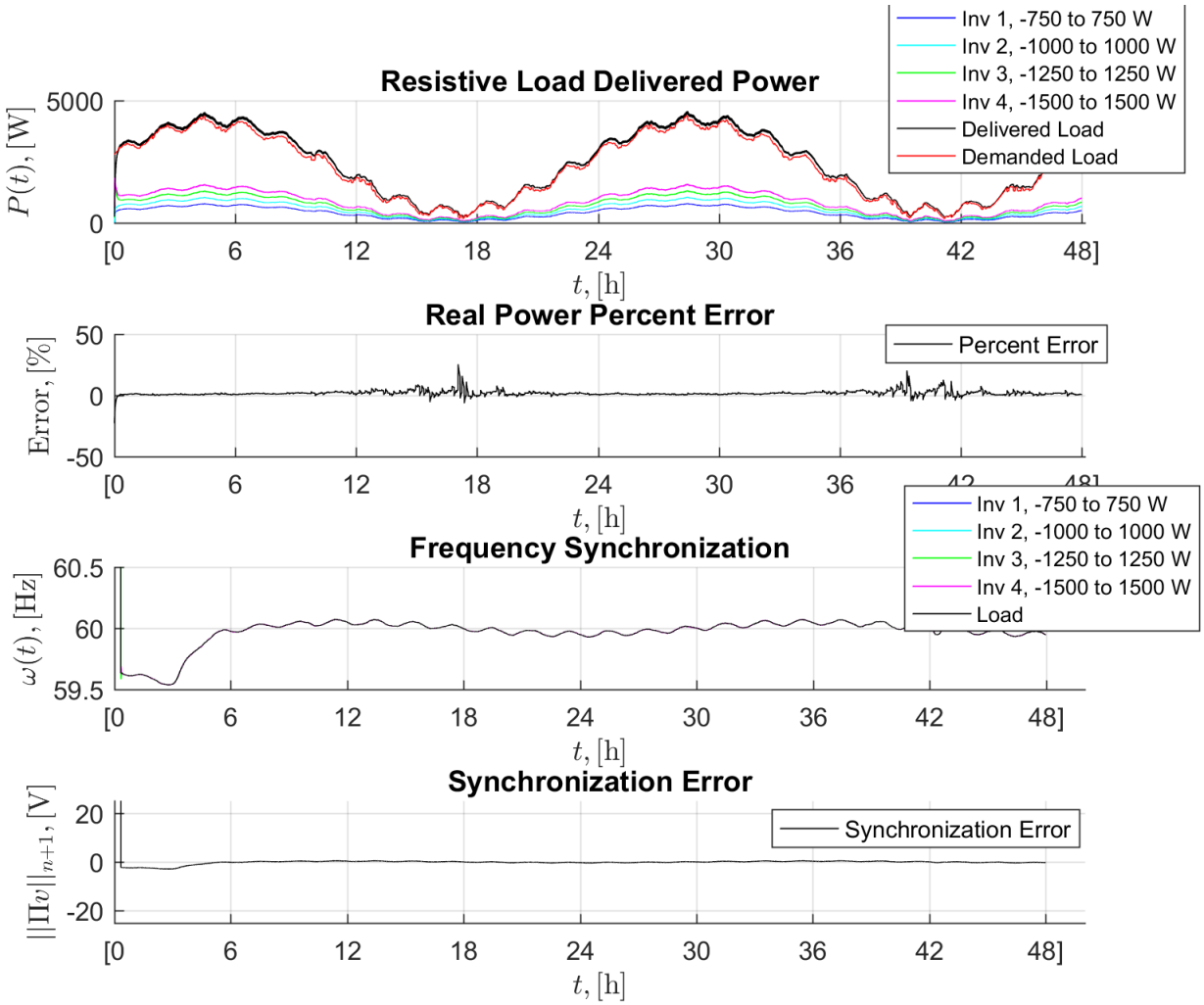

FIGURE 4.3: Simulation of four inverters under varying load with DAPI control despite load noise, demonstrating synchronicity with each other and return to nominal frequency ω_{nom}

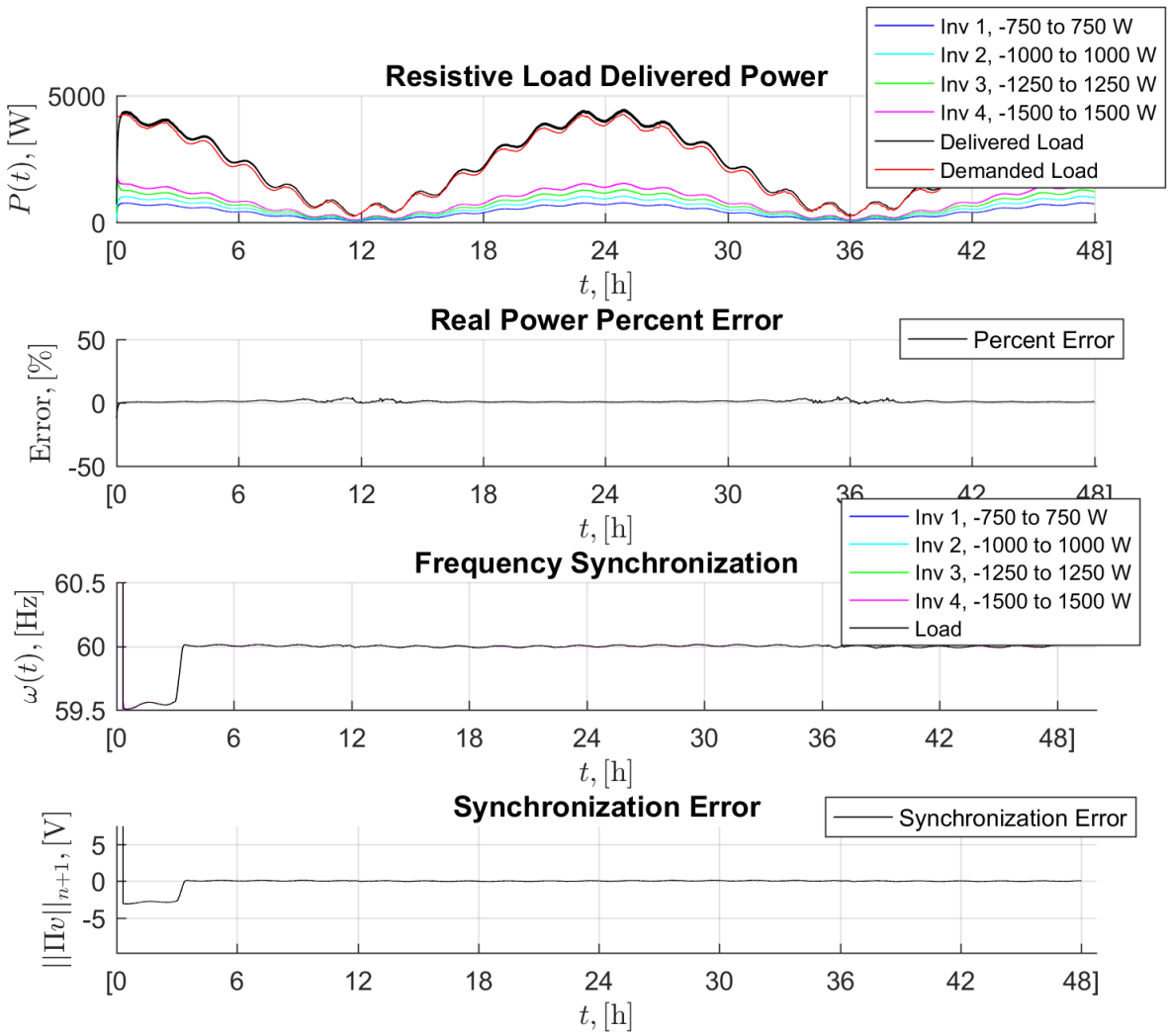

FIGURE 4.4: Simulation of four inverters under varying load with more aggressive DAPI control of $f_i = \frac{1}{10}$

4.3 Voltage Regulations

Now recall reactive power-voltage droop tradeoff:

$$V_i = V_{nom} - n_i Q_i \tag{1.2}$$

We borrow the droop coefficient n_i from equation (54) in [1]:

$$n_i = \frac{\kappa_v \kappa_i}{2\sigma} \left(\bar{V}_{oc} - \beta \bar{V}_{oc}^3\right)^{-1} \tag{4.14}$$

This gives a VOC reactive-power voltage droop tradeoff of

$$V_i = V_{nom} - \frac{\kappa_v \kappa_i}{2\sigma} \left(\bar{V}_{oc} - \beta \bar{V}_{oc}^3\right)^{-1} Q_i \tag{4.15}$$

To incorporate DAPI control for voltage correction, we follow a similar procedure. Begin with equations (7a) and (7b) from [12]:

$$V_i = V_{nom} + n_i Q_{eq} + e_i \tag{7a}$$

$$\frac{de_i}{dt} = -\frac{1}{g_i}\beta_i (V_i - V_{nom}) - \sum_{j=1}^{n} b_{ij} \left(\frac{Q_i}{Q_i^*} - \frac{Q_j}{Q_j^*}\right) \tag{7b}$$

As with equations (4.6) and (4.7), the first equation parallels the voltage droop relation in equation (1.2) with the addition of a secondary control variable e_i. The second equation describes the dynamics of the secondary controller, where g_i is a positive gain, β_i is a positive gain, and the $n \times n$ matrix B with elements $b_{ij} > 0$ describes the adjacency matrix of a communication network between nodes.

Consolidating the proposed DAPI controller and VOC droop coefficient give the following controller:

$$V_i = V_{nom} + \frac{\kappa_v \kappa_i}{2\sigma} \left(\bar{V}_{oc} - \beta \bar{V}_{oc}^3\right)^{-1} Q_{eq} + e_i \tag{4.16}$$

$$\frac{de_i}{dt} = -\frac{1}{g_i}\beta_i (V_i - V_{nom}) - \sum_{j=1}^{n} b_{ij} \left(\frac{Q_i}{Q_i^*} - \frac{Q_j}{Q_j^*}\right) \tag{4.17}$$

We incorporate the secondary controller's adjustment into the voltage scaling term κ_v, recalling equation (2.2):

$$\kappa_v = \bar{V}_{nom} \tag{2.2}$$

We let κ_v be

$$\kappa_v = \frac{\kappa_v \kappa_i}{2\sigma} \left(\bar{V}_{oc} - \beta \bar{V}_{oc}^3\right)^{-1} Q_{eq} + e_i \tag{4.18}$$

Figure 4.5 shows the results of a simulation of the now-familiar four inverters under DAPI control beginning at $t = 3$ seconds. The gain $g_i = 1$, $\beta_i = 1.2\ \forall i$, and the adjacency matrix B is $\mathbf{0_{4\times4}}$, implying that there is no second term. This corresponds to a case in which reactive power is shared poorly because the inverters do not coordinate the shifting of their droop curves according to their proportional ratings, resulting in the more dramatic error seen in the second subplot.

Figure 4.5 shows simulation results under the gains found from more precisely tuning the controller, which offer "a compromise between voltage regulation and reactive power sharing" [12]. The gain $g_i = 180$, $\beta_i = 1.2\ \forall i$, and the adjacency matrix B describes a communication network in which each node has two neighbors, quantified as:

$$\mathrm{B} = \begin{bmatrix} 0 & 1 & 0 & 1 \\ 1 & 0 & 1 & 0 \\ 0 & 1 & 0 & 1 \\ 1 & 0 & 1 & 0 \end{bmatrix}$$

Under this much faster and more communicative graph, the performance of the inverters with regards to synchronicity is much improved. Voltage synchronizes very tightly in less than a second after DAPI is turned on, and the synchronization error is very consistently near 0.

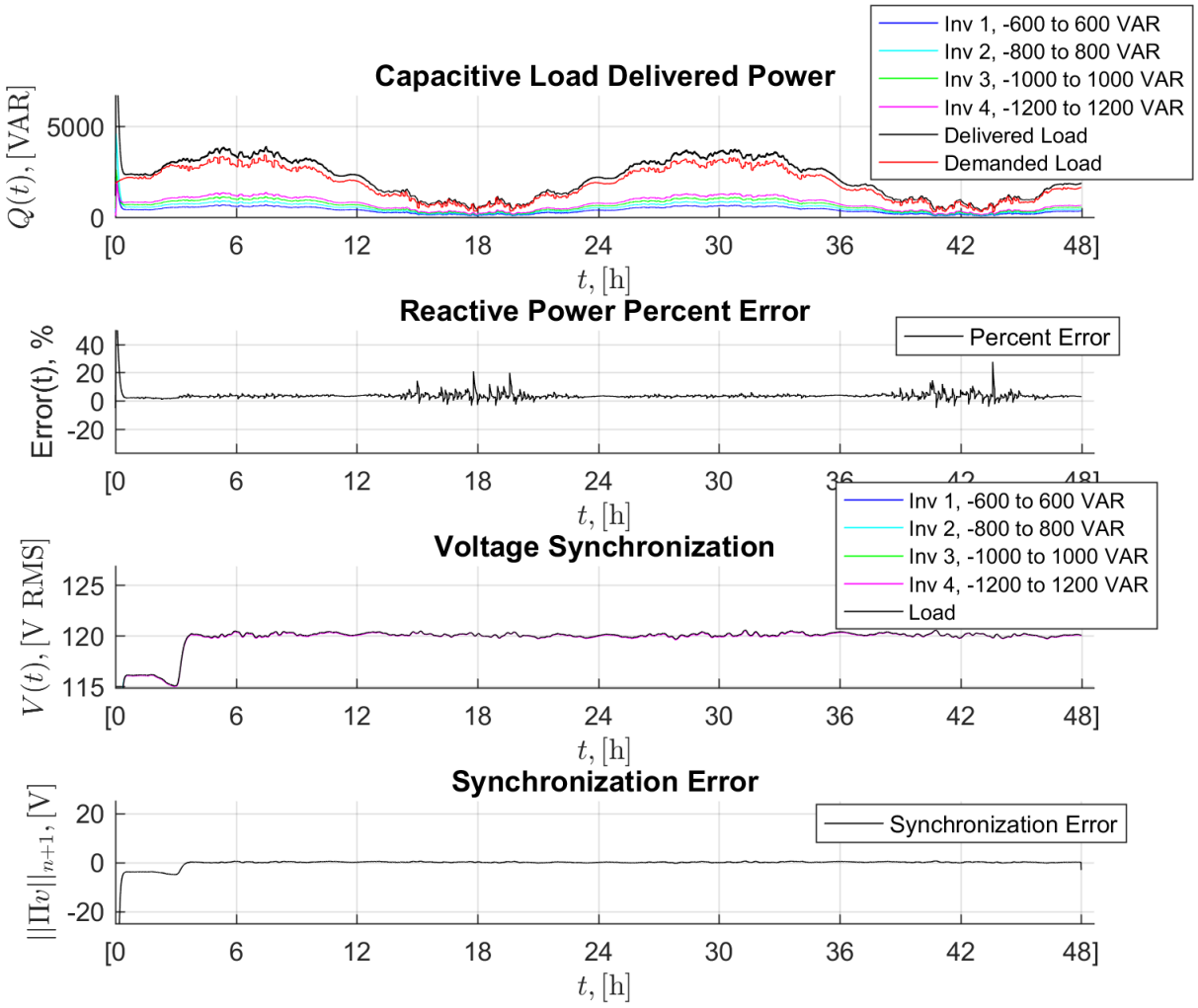

FIGURE 4.5: Simulation of four inverters under DAPI control $g_i = 1$, demonstrating synchronicity with each other and return to nominal voltage V_{nom} despite load noise

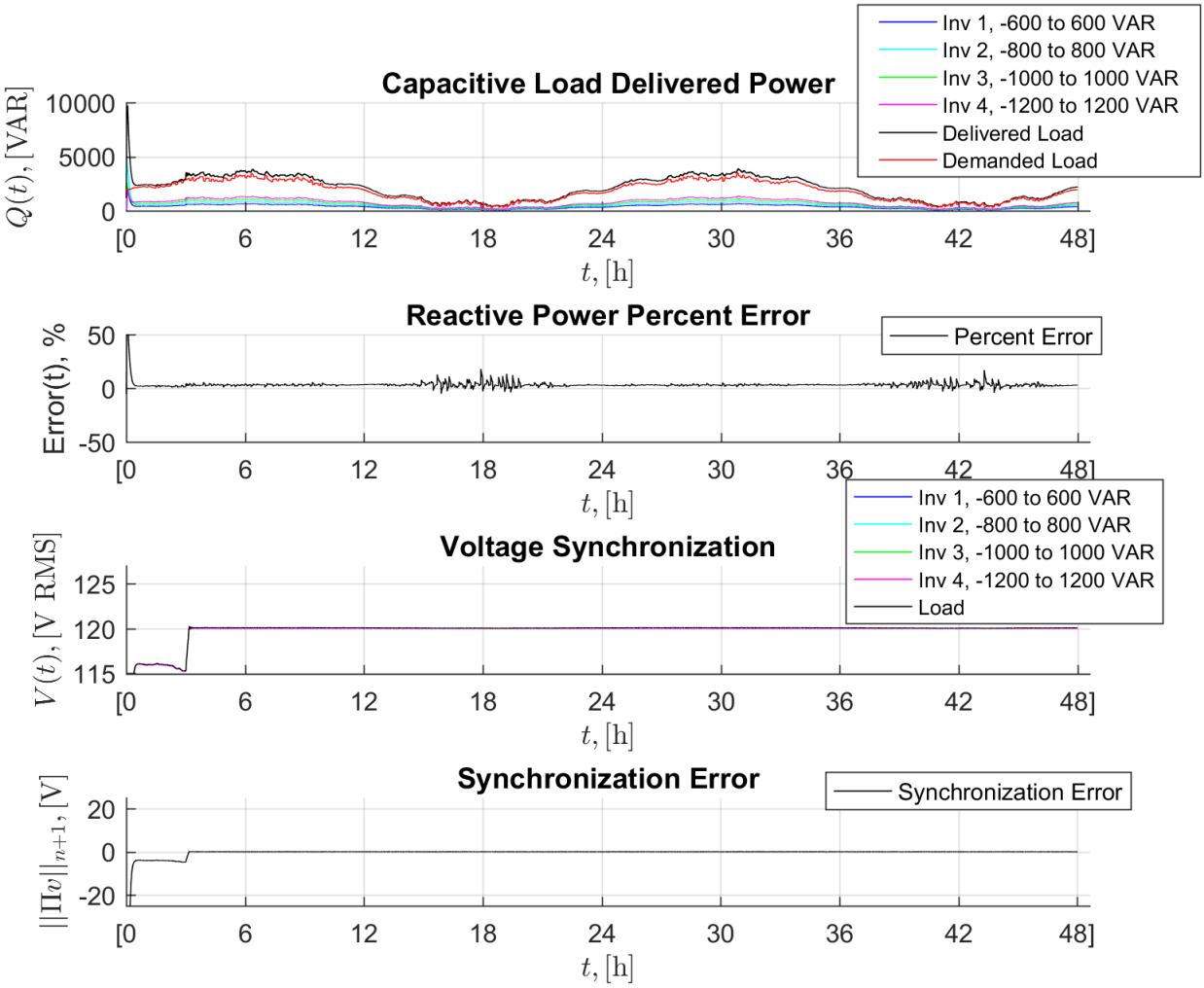

FIGURE 4.6: Simulation of four inverters under DAPI control with the "smart tuning" control gains from [12] of $g_i = 180$, $\beta_i = 1.2\ \forall i$, and a better networked adjacency matrix

Chapter 5

Energy Storage Systems

More accurately modeling batteries proves critical in reconciling simulation with reality, but inspection reveals that effective battery management systems (BMS) are also important in correctly informing the controller of a grid. Battery management systems serve to create a reliable, robust, cost-effective smart grid by protecting against deep charge/discharging of the batteries, minimizing degradation of battery efficiency by optimizing usage and providing more accurate estimates on batteries' state-of-charge (SOC) and state-of-health (SOH) to feedback systems [19]. Accurate representations of batteries' SOC is critical, for example, in ensuring that batteries are not dangerously overcharged or overdischarged.

The lithium-ion chemical composition is especially attractive for large-scale, distributed energy storage because of its energy density, response time, robustness to operating conditions, and technological maturity [4]. Lithium-ion is also especially attractive because Peukert's law, governing the change in capacity of rechargeable battery at different rates of discharge, is not applicable [20]. Generally, Peukert's law suggests that as the rate of discharge increases, so too does the battery's internal resistance, leading to a lower available total capacity. Lithium ion tends to self-heat during rapid discharge, and the Nernst Equation, foundational in the field of electrochemistry, predicts that battery voltage increases with temperature. Experimental results show that the self-heating offsets the loss in capacity–a 50Ah lithium-ion battery was discharged at 5 A and 50 A and found to have almost the same capacity [21]. Because of this, discussions of discharge rate, often refered to as C-rate, are excluded [22].

Because of Tesla's Powerwalls' market share and the availability of research analyzing their integration, the following simulations are based on characteristics of the lithium-ion based Tesla DC Powerwall. The system integration simulated follow directly from Tesla's suggested system layout for integrating a DC-coupled Powerwall System with a solar panel, shown in Figure 5.1. In these simulations, the inverter is assumed to be the virtual oscillator

controlled inverter, and the battery itself is assumed to have its own Energy Management System (EMS) control. For the purposes of this thesis, the EMS proposed will prioritize battery operation that optimizes the battery's long-term health, rather than battery optimization that concerns economic factors.

Much effort has been extended to characterize optimal controllers that incorporate economic factors. Analyses include weighing the cost between battery operation that compromises battery life but limits the utilization of expensive generation sources (such as coal) or demand-response systems in which a household is able to buy and sell energy from an electricity market. While these will certainly be important in future work, this is considered out of the scope of this work.

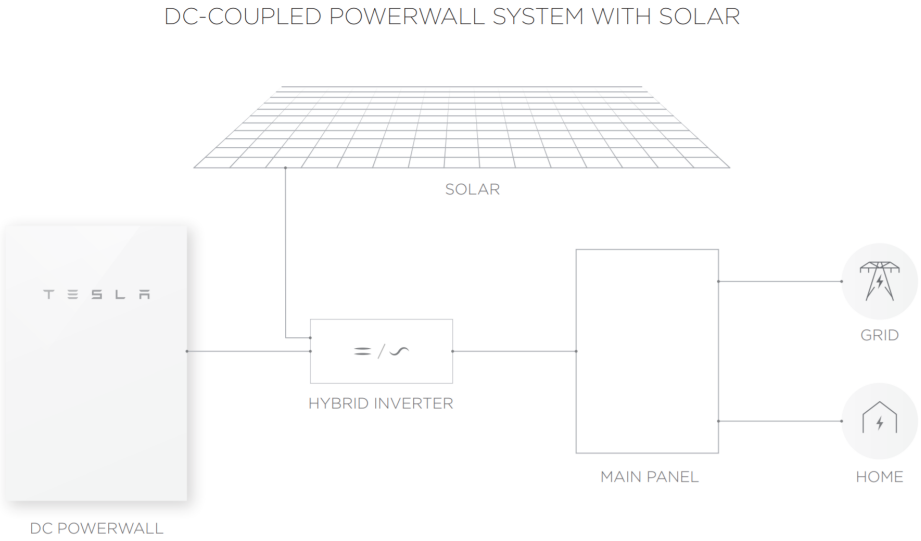

FIGURE 5.1: Tesla's DC Power Wall System Layout [23]

Table 5.1 details specific Tesla DC Powerwall parameters:

TABLE 5.1: Telsa Powerwall Specifications [23]

DC Energy [1]	13.5 kWH
Power, continuous	5 kW (charge and discharge)
Power, peak (10 sec)	7 kw (discharge only)
DC Voltage Range	350-550 V
DC Current, continuous	14.3 A
DC Current, peak (10 s)	20 A
Depth of discharge	100%
Round Trip Efficiency[1,2]	91.8%
Warranty	10 years

5.1 Battery Models

To build a more realistic model of a battery, accounting for details regarding battery chemistry, we begin from the simplest principles. Table 5.2 summarizes the main parameters that will be included in the models to follow, and Figure 5.2 visualizes an interconnection between an inverter and battery.

$\bar{P}_{rated,max,i}$ describes the maximum power that the inverter can output to the grid, limited by its physical characteristics. $P_{PV,max,i}(t)$ is the time-varying output available to the battery and inverter. Previously, this parameter had

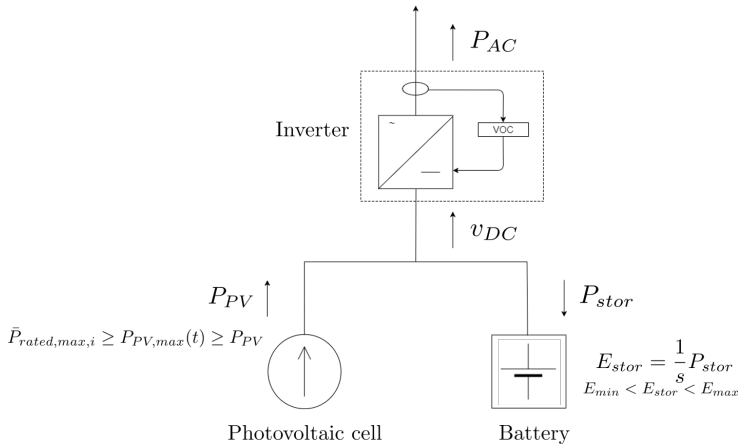

FIGURE 5.2: Connection between inverter and battery

been assumed to be greater than the demand on the system, but now, energy storage systems are included to compensate for deficits. $P_{AC,i}(t)$ is the proportional load for which the inverter is responsible. $P_{batt}(t)$ is the power entering or leaving the battery, with the convention that $P_{batt}(t) > 0$ corresponds to charging the battery and $P_{batt}(t) < 0$ corresponds to discharging the battery. Q_{min} reflects the minimum energy that can safely be stored in the battery before dealing with concerns of overdischarge, and Q_{max} is the maximum energy a battery can store. Lastly, $E_{batt}(t)$ is the energy stored in the battery at time t.

TABLE 5.2: Battery Parameters

Variable	Description
$\bar{P}_{rated,max,i}$	Inverter maximum deliverable power
$P_{PV,max,i}(t)$	Time-varying power generated
$P_{AC,i}(t) = P_{load}(t)\frac{\bar{P}_{rated,max,i}}{\sum_{k=1}^{n}\bar{P}_{rated,max,k}}$	Inverter i proportional load
$P_{batt}(t)$	Power entering/leaving battery
Q_{min}	Minimum battery energy capacity
Q_{max}	Maximum battery energy capacity
$Q_{min} < E_{batt}(t) < Q_{max}$	Battery energy

[1] Values provided for 25 C, 3.3 kW charge/discharge power

[2] DC to battery to DC, at beginning of life

From the most basic premise, a battery can be be modelled as a simple integrator of power draw:

$$E_{batt}(t) = f(P_{batt}(t)) = \frac{1}{s}P_{batt(t)} \tag{5.1}$$

Doing so captures the most basic dynamics of power consumption but is a gross oversimplification of power electronics with respect to both the physical properties of batteries and best practices for extending batteries' longevity.

With lithium ion batteries, for example, best practices indicate that charging and discharging with different currents can dramatically effect the energy available from the battery. Overdrawing the battery can decrease available energy. Every power cycle can reduce the batteries' capacities. The following section draws from various sources to create a more realistic battery model that incorporates these real-world physical factors.

Of particular interest is how lithium ion batteries age [24]. Processes such as electrolyte decomposition, compromised contacts at the cathode, and the formation of surface films on both electrodes can compromise a battery's capacity throughout its lifetime. A battery's performance will deteriorate as its internal resistance increases, which also means that its maximum capacity Q_{max} will decrease. This causes the parameter Q_{max} to become a function of cycles and operational conditions.

Decreases in discharge capacity can be described by equation (6.2) from [24]:

$$Q_{d,i}[\%] = 100\left(1 - \frac{Q_{d,i}^{j}}{Q_{max}}\right) \tag{5.2}$$

where $Q_{di}[\%]$ denotes the decrease in capacity Q_d [Ah] after j cycles of battery i. Tesla's DC Powerwall promises a warranty of 10 years, with an energy

retention of "70% at 10 years following initial installation date" for solar self-consumption and grid backup, with no operating limitations (i.e., unlimited cycles) [23], [25]. Assume approximately daily charging and discharging for 10 years for a total of 3,650 cycles. From an initial capacity Q_{max} of 13500 kWh, a correctly operated Powerwall will have a Q_d^j of 9450 Wh after 3,650 cycles. Manipulating equation 5.2 gives the relationship below to describe how Q_{max} changes with each battery cycle:

$$Q_{max}(j) = Q_{max}\left(1 - \frac{0.3 * j}{3650}\right) \tag{5.3}$$

where j is the number of cycles, approximately equal to days of operation. In the interest of reflecting real world conditions and in accordance with literature describing sufficient depths of discharge, the simulations to be shown reflect a full charge as a charge that spans from a State-of-Charge at a low of 30% to 70% [26].

5.2 Battery Controllers

Assume that the previous section describing the relationship between $E_{stor}(t)$ and $P_{stor}(t)$ holds true for the following discussion of battery management schemes.

Because the load must be serviced before the battery can be charged, we introduce a term that charges the battery in the event of excess power and draws from the battery if the power produced by the photovoltaic cell is insufficient to service the load.

$$P_{margin}(t) = P_{PV,max}(t) - P_{AC,i}(t) \tag{5.4}$$

where $P_{PV,max}(t)$ is the time-varying power available from the photovoltaic cell and the aforementioned $P_{AC,i}(t) = P_{load}(t)\frac{\bar{P}_{rated,max,i}}{\sum_{k=1}^{n}\bar{P}_{rated,max,k}}$ is the proportional load demanded from inverter i. This term $P_{margin}(t)$ ensures that the battery charges or discharges accordingly to whether or not the load is greater or less than the available power. If $P_{PV,max}(t)$ is greater than $P_{AC,i}(t)$, then the term will be positive, meaning that after the photovoltaic services the load, it still has excess power that can be used to charge the battery. If $P_{PV,max}(t)$ is less than $P_{AC,i}(t)$, then the term will be negative, meaning that the photovolatic does not have enough power to service the load and power must be drawn from the battery. Therefore let the power entering or leaving the battery first be simply a reflection of the available or demanded power:

$$P_{batt}(t) = P_{margin}(t) \tag{5.5}$$

To respect the upper and lower limits of the battery's energy capacity, respectively $E_{batt,min}$ and $E_{batt,max}$, we introduce the following controllers to limit power consumption and delivery:

$$P_{batt}(t) = P_{margin}(t)\left(\frac{Q_{max}(j) - E_{batt}(t)}{Q_{max}(j)}\right)\left(\frac{E_{batt}(t) - Q_{min}}{E_{batt}(t)}\right) \tag{5.6}$$

The first term limits power consumed by the battery as the battery becomes fully charged, while respecting the previous discussion of battery capacity degradation, and the second term limits the battery's discharge as the battery becomes depleted, to ensure that the battery does not dangerously overdischarge. Note that both act as scaling factors on $P_{margin}(t)$ and that each term is always between 0 and 1.

To incorporate parameters to reflect the asymmetrical charge and discharge profiles that the Powerwall can support, listed in Table 5.1, we introduce two additional parameters:

$$P_{chr,max} = 5000W \tag{5.7}$$

$$P_{dis,max} = 7000W \tag{5.8}$$

These upper and lower limits determine the power profile that the battery

can safely support. We incorporate them into our battery management as follows:

$$P_{batt}(t) = \begin{bmatrix} sat_0^{P_{chr,max}}\{P_{margin(t)}\} & sat_{P_{dis,max}}^{0}\{P_{margin(t)}\} \end{bmatrix} * \begin{bmatrix} \frac{Q_{max}(j)-E_{batt}(t)}{Q_{max}(j)} \\ \\ \frac{E_{batt}(t)-Q_{min}}{E_{batt}(t)} \end{bmatrix} \tag{5.9}$$

To understand this formulation, consider two examples. First imagine that more power is being generated than in being demanded, so $P_{margin}(t) > 0$. This causes $sat_0^{P_{chr,max}}\{P_{margin(t)}\}$ to either be equal to the available marginal power or to saturate at the upper limits of the battery's physical ability and causes $sat_{P_{dis,max}}^{0}\{P_{margin(t)}\}$ to saturate at 0. Therefore the row vector effectively becomes a scaled selection matrix of $\begin{bmatrix} P_{margin}(t) & 0 \end{bmatrix}$. The $P_{margin}(t)$ is then scaled by $\frac{Q_{max}(j)-E_{batt}(t)}{Q_{max}(j)}$, which curtails the power entering the battery as the battery becomes too full.

Although lithium ion's internal temperature tends to offset increases in internal resistance, the battery's operation is still susceptible to changes in external temperature. The temperature index of nominal capacity $c_\tau(\tau)$ is [27]:

$$c_\tau(\tau) = \frac{Q_\tau}{Q_{\tau n}} = \frac{1}{1 + \alpha|(\tau_n - \tau)|} \tag{5.10}$$

where Q_τ is the battery capacity as a function of temperature, $Q_{\tau n}$ is battery

capacity at nominal temperature, and we assume $\alpha \approx 0.01$ deg^{-1}. Assume the PV output $P_{PV,max}(t)$ correlates with irradiance, which affects temperature, so a derivation of temperature from PV output is as follows, where nominal temperature τ_n is 25 C as specified in the data sheet for the DC Power Wall [23] and is assumed to be 75% of the PV's maximum rated power $P_{rated,max,i}$:

$$\tau(t) = (P_{PV,max}(t) - 0.75 * P_{rated,max,i}) * \tau_n + \tau_n \tag{5.11}$$

Plugging this into equation 5.10:

$$c_\tau(\tau, t) = \frac{Q_\tau}{Q_{\tau n}} = \frac{1}{1 + 0.01|(\tau_n - ((P_{PV,max}(t) - 0.75 * P_{rated,max,i}) * \tau_n + \tau_n))|} \tag{5.12}$$

$$c_\tau(\tau) = \frac{1}{1 + 0.01|(P_{PV,max}(t) - 0.75 * P_{rated,max,i}) * \tau_n|} \tag{5.13}$$

5.3 Battery Simulation

Because batteries supply real power (rather than reactive power), capacitive loads are not simulated here. To show the full functionality of the batteries, generation is now simulated as a fluctuating sine wave, informed by literature on irradiance modeling and data from hourly photovoltaic power generation [28] [29].

Figure 5.3 shows the simulation results of the same four inverters, now equipped with four batteries emulating Tesla Powerwalls. The first subplot shows the available power in orange, the demanded power in red, and the delivered power in black. The second subplot shows the energy stored in the batteries, which tracks the difference between demanded and available energy. Lastly, the third subplot shows that the power injections are synchronizing.

Figure 5.4 shows the same simulation with an aggressive DAPI controller turned on at $t = 3$ seconds. Despite very noisy load and generation, the batteries operate as expected and the inverters' power injections synchronize to ω_{nom}.

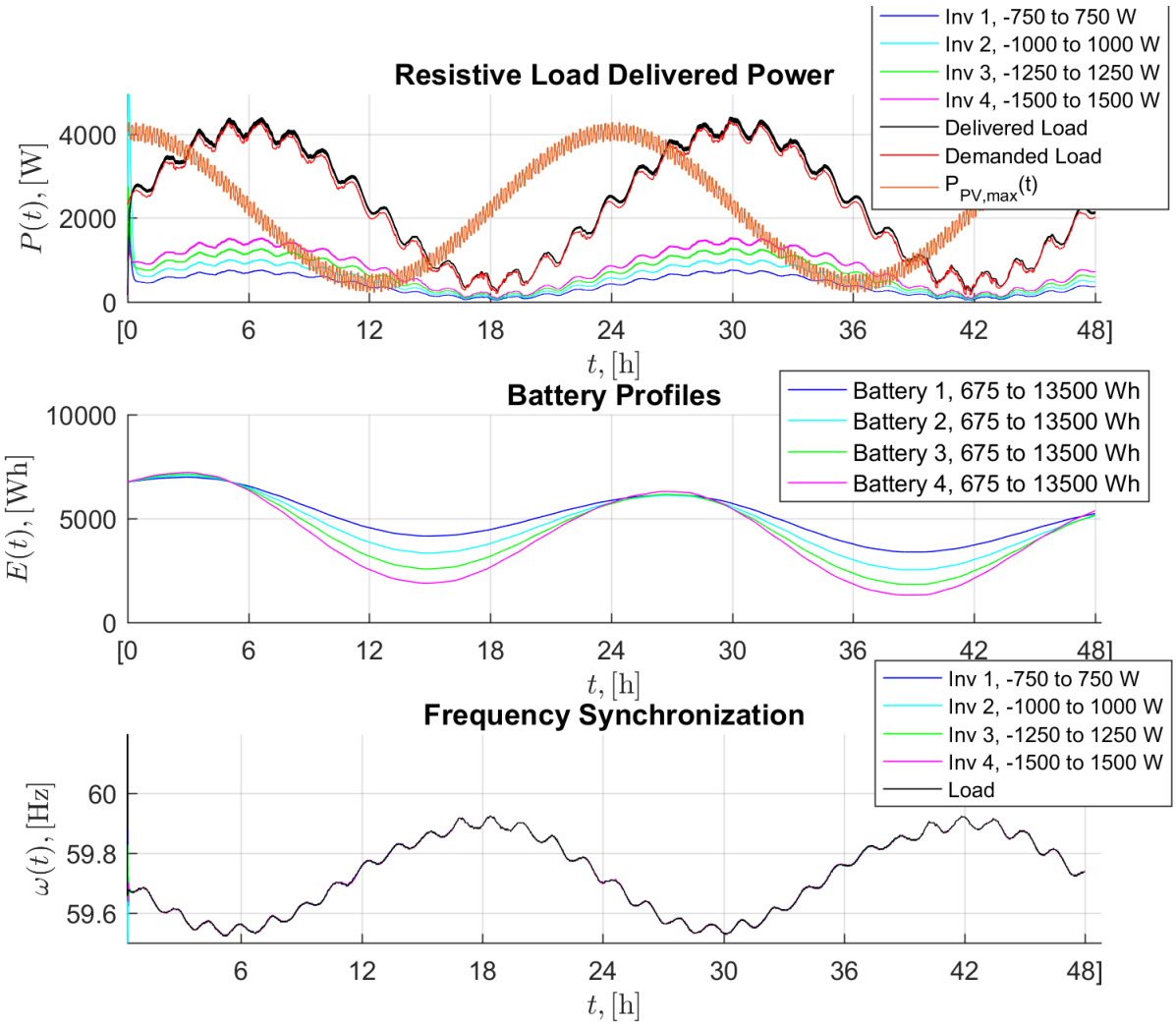

FIGURE 5.3: Simulation of four inverters equipped with batteries

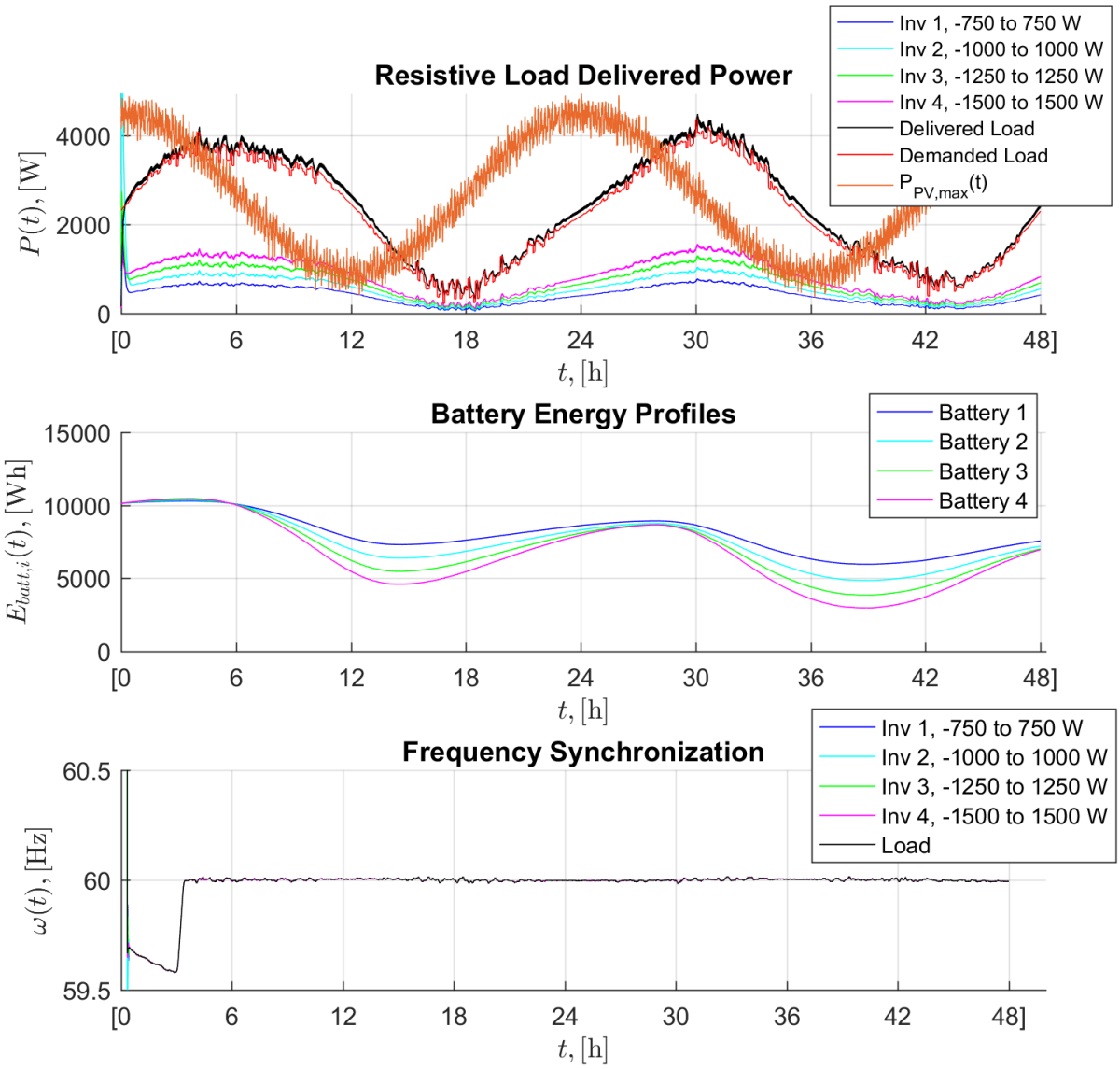

FIGURE 5.4: Simulation of four inverters equipped with batteries and DAPI control

Chapter 6

Conclusion

6.1 Summary of Results

As variable renewable energy generation sources become more prevalent sources of power, grid designers must anticipate the challenges that interfacing will present. Virtual Oscillator Control (VOC) proposes a real-time decentralized control strategy that mimics characteristics of the ubiquitous droop control but acts on a much faster time scale, making VOC a viable option for control fluctuating, noisy sources.

This work includes three contributions to research on VOC. Firstly, we simulate a collection of parallel inverters of varying size in a microgrid setting,

servicing fluctuating and noisy loads, and show that they perform well within tolerable margins. Secondly, we adapt a distributed averaging proportional integral (DAPI) control intended to correct for steady-state error in droop control and apply the secondary controller to a microgrid composed of VOC inverters. Simulations demonstrate that DAPI translates well to a VOC-based microgrid. Lastly, we design and incorporate energy storage systems (ESS) into a VOC-based microgrid. The ESS compensate for generation sources in periods of excess load relative to generation, providing margins on the total system capacity.

6.2 Future Work

Virtual Oscillator Control presents promising opportunities for better integrating variable renewable energy sources. Interesting future directions might involve characterizing microgrids in the presence of heterogenous control. For example, literature review yielded little substantial analysis of a system with secondary controllers implemented on only some inverters. While we conducted preliminary simulations to examine microgrid performance with some inverters using only VOC and others using VOC and DAPI, rigorous proofs of stability remain unclear.

Comparison of the battery models shown here against real-time ESS models would better inform future evolutions of controllers. Incorporating other elements of tertiary control, such as flexible demand or economic behavior shaping, would also be an interesting direction.

Bibliography

[1] Brian B. Johnson, Mohit Sinha, Nathan G. Ainsworth, Florian Dorfler, and Sairaj V. Dhople. "Synthesizing Virtual Oscillators to Control Islanded Inverters". *IEEE Transactions on Power Electronics*, 31(8):6002–6015, 2016. ISSN 08858993. doi: 10.1109/TPEL.2015.2497217.

[2] Florian Dorfler, John W. Simpson-Porco, and Francesco Bullo. "Breaking the hierarchy: Distributed control and economic optimality in Microgrids". *IEEE Transactions on Control of Network Systems*, 3(3):241–253, 2016. ISSN 23255870. doi: 10.1109/TCNS.2015.2459391.

[3] H. Han, Y. Liu, Y. Sun, M. Su, and J. M. Guerrero. An improved droop control strategy for reactive power sharing in islanded microgrid. *IEEE Transactions on Power Electronics*, 30(6):3133–3141, June 2015. ISSN 0885-8993. doi: 10.1109/TPEL.2014.2332181.

[4] Holger C. Hesse, Michael Robert Schimpe, Daniel Kucevic, and Andreas Jossen. Lithium-ion battery storage for the grida review of stationary battery storage system design tailored for applications in modern power grids. 2017.

[5] Hedi Bouattour. Distributed secondary control in microgrids. Master's thesis, University of California, Santa Barbara, 2013.

[6] Dan T. Ton and Merrill A. Smith. "the u.s. department of energy's microgrid initiative". *The Electricity Journal*, 25(8):84 – 94, 2012. ISSN 1040-6190. doi: https://doi.org/10.1016/j.tej.2012.09.013. URL http://www.sciencedirect.com/science/article/pii/S1040619012002254.

[7] Qing-Chang Zhong and Tomas Hornik. *Control of power inverters in renewable energy and smart grid integration*. J. Wiley Sons-IEEE Press, Chichester, 2012. URL http://cds.cern.ch/record/1555098.

[8] Alaa Mohd, Egon Ortjohann, Danny Morton, and Osama Omari. "review of control techniques for inverters parallel operation". *Electric Power Systems Research*, 80(12):1477 – 1487, 2010. ISSN 0378-7796. doi: https://doi.org/10.1016/j.epsr.2010.06.009. URL http://www.sciencedirect.com/science/article/pii/S0378779610001392.

[9] Ward Bower, Ross Guttromson, Steve Glover, Jason Stamp, and Dhruv Bhatnagar. "the advanced microgrid: Integration and interoperability".

[10] John W. Simpson-Porco, Florian Drfler, and Francesco Bullo. Synchronization and power sharing for droop-controlled inverters in islanded microgrids. *Automatica*, 49(9):2603 – 2611, 2013. ISSN 0005-1098. doi: https://doi.org/10.1016/j.automatica.2013.05.018. URL http://www.sciencedirect.com/science/article/pii/S0005109813002884.

[11] P. Kundur. *Power System Stability And Control*. EPRI power system engineering series. 1994. ISBN 9780070635159. URL https://books.google.com/books?id=v3RxH_GkwmsC.

[12] IEEE JohnW. Simpson-Porco, Student Member, IEEE, Qobad Shafiee, Member, IEEE, Florian Dörfler, Member, IEEE, Juan C. Vasquez, Senior Member, IEEE, Josep M. Guerrero, Fellow, IEEE, and Francesco Bullo, Fellow. "Secondary Frequency and Voltage Control of Islanded Microgrids via Distributed Averaging Secondary Frequency and Voltage Control of Islanded Microgrids via Distributed Averaging"". 62(April 2016):7025–7038, 2015. doi: 10.1109/TIE.2015.2436879.

[13] Mohit Sinha, Florian Dorfler, Brian B. Johnson, and Sairaj V. Dhople. Uncovering Droop Control Laws Embedded Within the Nonlinear Dynamics of Van der Pol Oscillators. pages 1–12, 2014. URL http://arxiv.org/abs/1411.6973.

[14] B. B. Johnson, S. V. Dhople, A. O. Hamadeh, and P. T. Krein. Synchronization of parallel single-phase inverters with virtual oscillator control. *IEEE Transactions on Power Electronics*, 29(11):6124–6138, Nov 2014. ISSN 0885-8993. doi: 10.1109/TPEL.2013.2296292.

[15] B. B. Johnson, S. V. Dhople, A. O. Hamadeh, and P. T. Krein. Synchronization of nonlinear oscillators in an lti electrical power network. *IEEE Transactions on Circuits and Systems I: Regular Papers*, 61(3):834–844, March 2014. ISSN 1549-8328. doi: 10.1109/TCSI.2013.2284180.

[16] Mohit Sinha, Sairaj Dhople, Brian Johnson, Nathan Ainsworth, and Florian Dörfler. Nonlinear supersets to droop control. *2015 IEEE 16th Workshop on Control and Modeling for Power Electronics, COMPEL 2015*, 2015. doi: 10.1109/COMPEL.2015.7236441.

[17] F. Wang, J. L. Duarte, and M. A. M. Hendrix. Active and reactive power control schemes for distributed generation systems under voltage

dips. In *2009 IEEE Energy Conversion Congress and Exposition*, pages 3564–3571, Sept 2009. doi: 10.1109/ECCE.2009.5316564.

[18] Pamela MacDougall, Cor Warmer, and Koen Kok. Mitigation of wind power fluctuations by intelligent response of demand and distributed generation. In *Innovative Smart Grid Technologies (ISGT Europe), 2011 2nd IEEE PES International Conference and Exhibition on*, pages 1–6. IEEE, 2011.

[19] Anna Stefanopoulou. Control engineers: the unsung heroes of battery technology. In *56th IEEE Conference on Control and Decision Plenary Speaker*, 2017.

[20] Yongyao Xia, Yunhong Zhou, and Masaki Yoshio. Capacity fading on cycling of 4 v li limno cells. 144:2593, 08 1997.

[21] Dennis Doerffel and Suleiman Abu Sharkh. A critical review of using the peukert equation for determining the remaining capacity of lead-acid and lithium-ion batteries. *Journal of Power Sources*, 155(2):395 – 400, 2006. ISSN 0378-7753. doi: https://doi.org/10.1016/j.jpowsour.2005.04.030. URL http://www.sciencedirect.com/science/article/pii/S0378775305007093.

[22] Henk Jan Bergveld, Wanda S. Kruijt, and Peter H. L. Notten. *Battery Management Systems*, pages 9–30. Springer Netherlands, Dordrecht, 2002. ISBN 978-94-017-0843-2. doi: 10.1007/978-94-017-0843-2_2. URL https://doi.org/10.1007/978-94-017-0843-2_2.

[23] Tesla powerwall data dc sheet. . URL https://www.solahart.com.au/media/2849/powerwall-2-dc_datasheet_english.pdf.

[24] Valer Pop. *Battery management systems: accurate state-of-charge indication for battery powered applications*. Springer, 2008.

[25] Tesla powerwall 2 dc limited warranty (usa). . URL https://www.tesla.com/sites/default/files/pdfs/powerwall/Powerwall_2_DC_Warranty_USA_1-1.pdf.

[26] Sven van der Kooij, PL Kempker, JL van den Berg, and Sandjai Bhulai. *Optimal charging/discharging strategies for batteries in smart energy grids*. Master's thesis, Vrije Universiteit Amsterdam.

[27] Antoni Szumanowski and Yuhua Chang. Battery management system based on battery nonlinear dynamics modeling. *IEEE Transactions on Vehicular Technology*, 57:1425–1432, 2008.

[28] Christopher T. M. Clack. Modeling solar irradiance and solar pv power output to create a resource assessment using linear multiple multivariate regression. *Journal of Applied Meteorology and Climatology*, 56(1):109–125, 2017. doi: 10.1175/JAMC-D-16-0175.1. URL https://doi.org/10.1175/JAMC-D-16-0175.1.

[29] H. P. Hellman, M. Koivisto, and M. Lehtonen. Photovoltaic power generation hourly modelling. In *Proceedings of the 2014 15th International Scientific Conference on Electric Power Engineering (EPE)*, pages 269–272, May 2014. doi: 10.1109/EPE.2014.6839426.